UC Irvine
UC Irvine Previously Published Works

Title

High Glucose Triggers Nucleotide Imbalance through O-GlcNAcylation of Key Enzymes and Induces KRAS Mutation in Pancreatic Cells

Permalink

https://escholarship.org/uc/item/17k199v6

Journal

Cell Metabolism, 29(6)

ISSN

1550-4131

Authors

Hu, Chun-Mei

Tien, Sui-Chih

Hsieh, Ping-Kun

et al.

Publication Date

2019-06-01

DOI

10.1016/j.cmet.2019.02.005

Copyright Information

Peer reviewed

High Glucose Triggers Nucleotide Imbalance through O-GlcNAcylation of Key Enzymes and Induces KRAS Mutation in Pancreatic Cells

Chun-Mei Hu,[1,7,*] Sui-Chih Tien,[1] Ping-Kun Hsieh,[1] Yung-Ming Jeng,[2] Ming-Chu Chang,[3] Yu-Ting Chang,[3] Yi-Ju Chen,[4] Yu-Ju Chen,[4] Eva Y.-H.P. Lee,[5] and Wen-Hwa Lee[1,6,*]

[1]Genomics Research Center, Academia Sinica, Taipei 11529, Taiwan
[2]Department of Pathology, National Taiwan University Hospital, Taipei 10041, Taiwan
[3]Department of Internal Medicine, National Taiwan University Hospital, Taipei 10041, Taiwan
[4]Institute of Chemistry, Academia Sinica, Taipei 11529, Taiwan
[5]Department of Biological Chemistry, University of California, Irvine, Irvine, CA 92697, USA
[6]Drug Development Center, China Medical University, Taichung 40402, Taiwan
[7]Lead Contact
*Correspondence: cmhu1220@gate.sinica.edu.tw (C.-M.H.), whlee@uci.edu (W.-H.L.)
https://doi.org/10.1016/j.cmet.2019.02.005

SUMMARY

KRAS mutations are the earliest events found in approximately 90% of pancreatic ductal adenocarcinomas (PDACs). However, little is known as to why *KRAS* mutations preferentially occur in PDACs and what processes/factors generate these mutations. While abnormal carbohydrate metabolism is associated with a high risk of pancreatic cancer, it remains elusive whether a direct relationship between *KRAS* mutations and sugar metabolism exists. Here, we show that under high-glucose conditions, cellular O-GlcNAcylation is significantly elevated in pancreatic cells that exhibit lower phosphofructokinase (PFK) activity than other cell types. This post-translational modification specifically compromises the ribonucleotide reductase (RNR) activity, leading to deficiency in dNTP pools, genomic DNA alterations with *KRAS* mutations, and cellular transformation. These results establish a mechanistic link between a perturbed sugar metabolism and genomic instability that induces *de novo* oncogenic *KRAS* mutations preferentially in pancreatic cells.

INTRODUCTION

Pancreatic cancer is a serious health issue in developed countries (Siegel et al., 2016). Pancreatic ductal adenocarcinoma (PDAC) accounts for 95% of all pancreatic cancers and is the most aggressive human malignancy with clinical features of local invasion, early metastasis, and resistance to standard chemotherapy (Campbell et al., 2010; Notta et al., 2016). Lack of both early detection and appropriate targeted therapies contributes to the extremely low survival rate of PDAC patients (Siegel et al., 2016).

The development of PDAC is characterized by a series of gene mutations. Among these, lesions in the *KRAS* gene are the earliest and most frequent alterations, occurring in 94% of PDAC patient samples (Hezel et al., 2006; Waters and Der, 2018). Mutated KRAS can be readily activated by upstream stimulants, leading to prolonged and strong KRAS activity (Eser et al., 2014; Huang et al., 2014) that is critical for reprogramming glucose, glutamine, and nucleotide metabolism to facilitate rapid proliferation of cancer cells (Bryant et al., 2014; Ying et al., 2012). In addition, turning off mutant *KRAS* expression through use of an inducible oncogenic *KRAS*[G12D] mouse model of PDAC demonstrated that *KRAS* mutation is essential for both PDAC initiation and maintenance *in vivo* (Collins et al., 2012; Ying et al., 2012). Although many studies suggested that mutation of the *KRAS* gene is a crucial step for PDAC development, how *KRAS* mutation is triggered, why the mutation frequency of *KRAS* gene is preferentially high in PDAC, and what processes or factors are involved in *KRAS* mutations remain largely unknown.

Based on the location and the physiological roles of the pancreas in modulating carbohydrate, protein, and lipid metabolism, the most likely risk factors are from metabolites. (Longnecker, 2014; Wellen and Thompson, 2010). Circumstantial evidence suggests that high, glucose-induced metabolism imbalance is associated with an elevated risk of pancreatic cancer (Aggarwal et al., 2013; Liao et al., 2015; Pannala et al., 2008; Vigneri et al., 2009). However, direct evidence linking sugar metabolism and genomic instability, including gene mutation in pancreatic cells, has yet to be established.

RESULTS

Metabolic Disorder of Sugar Triggers DNA Damage Preferentially in Pancreas

To explore this question, we first assessed DNA damage using immunohistochemical analyses with a γH2AX antibody as an indicator for genomic lesions and instability (Bonner et al., 2008; Valdiglesias et al., 2013) in tissues from tumor-free regions of the pancreas and intestines of PDAC patients with or without prior diagnosis of long-standing diabetes mellitus (DM). The patients' HbA1c and blood glucose levels were collected and
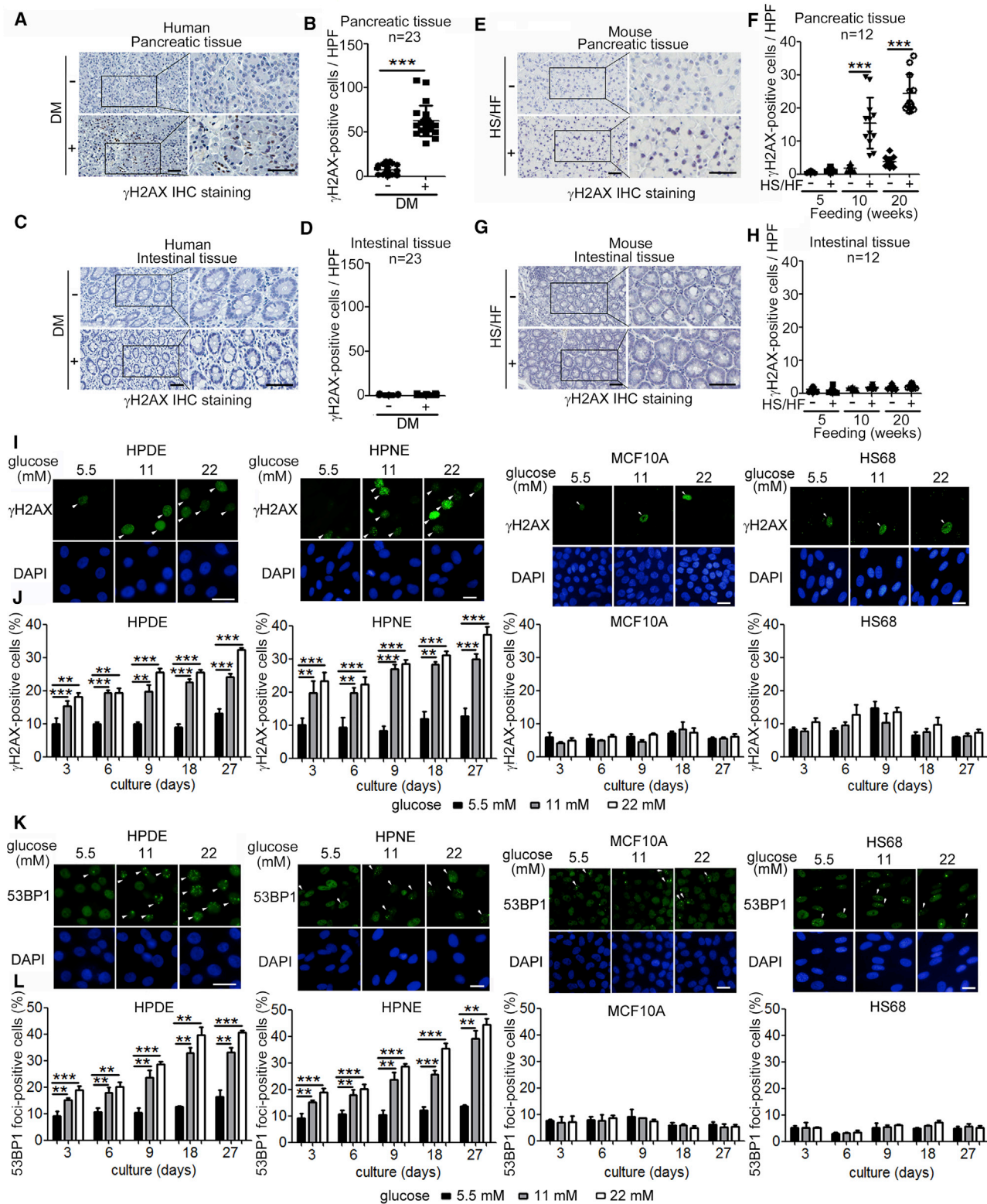
Figure 1. High Glucose in Pancreatic Cells Induces DNA Damage

(A–D) Representative images and quantification of γH2AX staining by immunohistochemistry (IHC) in pancreatic tissues (A and B) and small intestinal tissues (C and D) collected from PDAC patients with or without prior diagnosis of long-standing diabetes mellitus (DM). Each dot represents the datum from one patient. Scale bar, 50 μm. Values show mean ± SD (n = 23). High power field (HPF): 40× magnification.

confirmed as DM (Figures S1A and S1B). Interestingly, patients with DM had significantly more DNA damage in the pancreatic sections than patients without DM (Figures 1A and 1B), while there was no difference in the small intestinal sections (Figures 1C and 1D). To confirm this observation, we used C57BL/6 mice that were fed a high-sugar, high-fat (HS/HF) diet for 5, 10, and 20 weeks to induce metabolic disorders (Surwit et al., 1995). As expected, these mice showed a higher level of fasting blood glucose and increased body weight compared to those fed a standard chow diet (Figures S1C and S1D). Tissue samples from their pancreas, small intestine, colon, liver, lung, and kidney were collected at the indicated time points, and sections of each organ were prepared and immunohistochemically stained with antibodies against γH2AX. Positive staining was clearly observed in the pancreatic sections of mice fed the HS/HF diet for 20 weeks but not in the other tissue sections or in mice fed the chow diet (Figures 1E–1H, S1E, and S1F). These results suggest that metabolic disorders preferentially promote DNA damage in the pancreas.

To pinpoint which metabolite is the major culprit in causing DNA damage in the pancreas, two non-tumorigenic pancreatic cell lines, HPDE and HPNE, were cultured with high concentrations of glucose, glutamine (a representative for amino acids), or palmitic acid (a representative for saturated fatty acids) for 3 days, and then, DNA damage was examined using γH2AX foci as an indicator. Interestingly, the high-glucose treatment, but not glutamine or palmitic acid, efficiently increased DNA damage (Figures S1G–S1J). Similar observations were obtained by examining 53BP1 foci (Schultz et al., 2000), another marker for DNA damage and genomic instability (Figures 1I–1L) after treating with high concentrations of glucose (11 or 22 mM) for 3–27 days. On the other hand, high fructose induced less DNA damage compared to high glucose (Figure S1K). Interestingly, high-glucose treatment showed little effect on cell growth, cell cycle progression (Figures S1L and S1M), or cell survival (Figures S1N and S1O) in these pancreatic cell lines. Furthermore, several non-tumorigenic cell lines (i.e., two mammary epithelial cell lines, MCF10A and H184B5F5M10; one colon epithelial cell line, NCM356; one lung epithelial cell line, NL-20; and one foreskin fibroblast cell line, HS68) were examined, and these cell lines were insensitive to high-glucose-induced DNA damage (Figures 1I–1L and S1P–S1S), suggesting that this high-glucose-induced effect occurs preferentially in pancreatic cells.

The Incidence of *KRAS* Mutations Is Preferentially Elevated in Pancreatic Cells Treated with High Glucose
Gene alterations including single nucleotide variants (SNVs) are initiated by DNA damage (genomic instability) and the result of imbalance between DNA damage and repair. To examine whether the genomic alterations indicated by the γH2AX foci

are associated with *KRAS* mutations, we performed next-generation sequencing (NGS) of all exons of the *KRAS* gene in pancreatic tissues of PDAC patients with/without DM and in small intestinal tissues of PDAC patients with/without DM. Comparing similar reads per nucleotide after deep sequencing 40,000 to 50,000 times, the average of SNVs in the *KRAS* gene was significantly higher in the pancreatic tissues of PDAC patients with DM than in the other three tissue samples (Figures 2A and S2A). Similarly, the average of SNVs in the *Kras* gene was also significantly higher in pancreatic tissues of mice fed the HS/HF diet but not in small intestinal tissues or in pancreatic tissues of mice fed the chow diet (Figures 2B and S2D). However, the average of SNVs in the *GAPDH* or *Gapdh* gene showed no significant difference in the pancreatic and small intestinal tissues of patients or mice (Figures S2B, S2C, S2E, and S2F). Consistently, the average of SNVs in the *KRAS* gene was increased in HPDE, HPNE, and mouse primary acinar cells treated with high glucose but not in MCF10A and NL-20 cells (Figures 2C and 2D), while the average of SNVs in the *GAPDH* gene showed no significant difference among these cells (Figures S2G–S2L). These results indicate that high-glucose-induced genomic alterations occur preferentially in pancreatic cells and contain mutations in the *KRAS* gene.

Since 87% of the oncogenic *KRAS* mutations in PDAC patients are at amino acid G12 (Biankin et al., 2012) and 41% of those are *KRAS*^{G12D}, we used a specific antibody recognizing KRAS^{G12D}, as confirmed by immunofluorescence staining and cytometric analysis (Figures S2M and S2N), to detect the mutations induced by high glucose. As shown in Figure 2E, the numbers of KRAS^{G12D}-positive cells were increased in a time- and dose-dependent manner in both HPDE and HPNE cells with high-glucose treatment but not in MCF10A, H184B5F5M10, and HS68 cells. Similar results were obtained in high-glucose-treated mouse primary acinar cells, indicating that high glucose indeed induced the oncogenic *KRAS*^{G12D} mutation (Figures 2F and S2O). Furthermore, to test whether high glucose initiates *de novo* oncogenic *KRAS*^{G12D} mutation, approximately 200–300 HPDE cells were grown on coverslips to form individual colonies and simultaneously treated with 5.5, 11, or 22 mM glucose for 12 days. These colonies were then stained with the KRAS^{G12D} antibody, and the numbers of KRAS^{G12D}-positive cells in each colony were counted. As shown in Figure 2G, positive-staining cells were detected sporadically in multiple colonies rather than being enriched in single colonies. Nevertheless, the numbers of colonies with KRAS^{G12D}-positive cells were increased in samples from the high-glucose group (Figure 2H), indicating that high glucose initiated *de novo* *KRAS*^{G12D} mutation. The frequency of *de novo* KRAS^{G12D}-positive cells in the high-glucose-treated cells was about five-times more than that of the control cells (Figure 2I). Through

---

(E–H) Representative images and quantification of γH2AX staining by IHC in pancreatic tissues (E and F) and small intestinal tissues (G and H) collected from mice fed the chow diet or high-sugar and high-fat (HS/HF) diet. Each group contained 12 mice at indicated time points. Images shown: 20 weeks after feeding. Each dot represents the datum from one mouse. Scale bar, 50 μm. Values show mean ± SD.

(I–L) Representative images and quantification of γH2AX foci (I and J) and 53BP1 foci (K and L) staining by immunofluorescence (IF) in HPDE, HPNE, MCF10A, and HS68 cells cultured with the indicated concentrations of glucose for designated days. Images shown: 9 days after culture. 2,000 cells were counted in each experiment, and each assay was performed individually 4 times. White arrows indicate cells showing DNA breaks. Scale bar, 20 μm. Values show mean ± SD. *p < 0.05, **p < 0.01, ***p < 0.001 (two-tailed Student's t test).
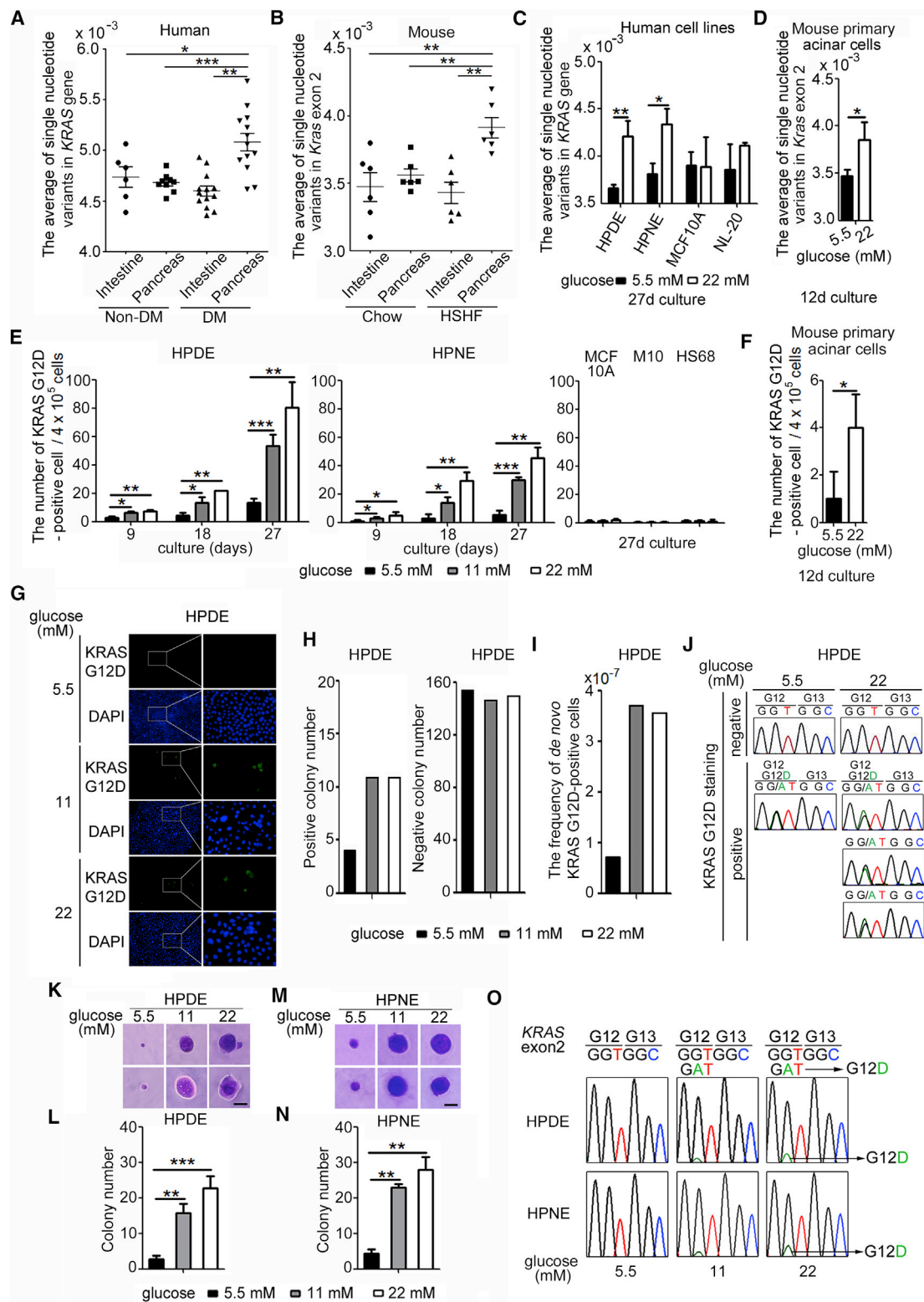
See also Figure S1.

Figure 2. High Glucose Triggers *KRAS* Mutations and Anchorage-Independent Growth in Pancreatic Cells

(A) The average of single nucleotide variants in the *KRAS* gene in small intestinal tissues and pancreatic tissues collected from PDAC patients with or without prior diagnosis of long-standing DM was determined by next-generation sequencing with Illumina Miseq. Pancreatic tissues and intestinal tissues from DM patients (n = 13); pancreatic tissues and intestinal tissues from non-DM patients (n = 9 and 6, respectively). Each dot represents the datum from one patient.

intracellular staining with the KRAS^{G12D} antibody, cell sorting, single-cell PCR with *KRAS* exon 2 primers, and Sanger sequencing, we confirmed that the *KRAS*^{G12D} mutation was present in these cells after high-glucose treatment (Figure 2J). Furthermore, we examined the effects of high glucose on cell transformation by performing soft agar colony formation assays and found that high glucose significantly promoted anchorage-independent growth of HPDE and HPNE cells, but not other types of cells (Figures 2K–2N and S2Q–S2X). Importantly, oncogenic *KRAS* mutations were acquired in these HPDE and HPNE colonies (Figure 2O). Since cells with oncogenic *KRAS* mutation appeared to have growth advantages in culture, we then tested whether growth selection pressure causes the increased frequency of *KRAS* mutation under high glucose. We performed a cell growth assay using primary pancreatic cells derived from PDX1-Cre; LSL-Kras$^{+/+}$ mice, and compared with that of from PDX1-Cre;LSL-Kras$^{G12D/+}$ mice. It was noted that the cells with oncogenic *Kras*^{G12D} mutation have a slight growth advantage compared to the cells with the wild-type *Kras* gene under either high or normal glucose conditions (Figure S2P), implicating that growth selection pressure may partially contribute to the increased frequency of *Kras* mutation. Taken together, these results suggest that the incidence of oncogenic *KRAS* mutations is significantly elevated and occurred preferentially in pancreatic cells following high-glucose treatment.

The dNTP Pools in Pancreatic Cells Are Disturbed with High-Glucose Treatment

To dissect the mechanism of how high glucose induces DNA damage in pancreatic cells, we examined two mechanisms of DNA damage including ROS-mediated oxidative stress (Cooke et al., 2003; Jena, 2012) and nucleotide imbalance-induced replication stress (Mathews, 2015; Zeman and Cimprich, 2014). We first used 2′,7′-Dichlorodihydrofluorescein diacetate (H$_2$DCFDA) staining to detect ROS levels in pancreatic, breast, and foreskin fibroblast cells after high-glucose treatment for 3 and 9 days and there was no consistent difference in ROS levels among these cells (Figure S3A). Next, we analyzed cellular nucleoside triphosphate (NTP) and deoxyribonucleotide triphosphate (dNTP) levels and found that high-glucose treatment dramatically reduced the levels of each dNTP, but not NTPs, in HPDE and HPNE cells, while this was not observed in other types of cells (Figures 3A

and S3B–S3D, and S3E and S3F). To test whether the reduction of dNTP pools contributes to the high-glucose-induced effects in pancreatic cells, we added extra amounts of ribonucleosides (N) and deoxynucleosides (dN) into the culture medium and observed that the high-glucose-induced effects were subdued (Figures 3B–3F, S3G, and S3H). Restoration of dNTP pools and reduction of DNA damage were similarly observed in mouse primary acinar cells supplemented with dN (Figures S3I–S3K). Taken together, these results suggest that high-glucose treatment decreases dNTP pools particularly in pancreatic cells, which might cause replication stress to increase mutations including oncogenic *KRAS*^{G12D}, and consequently promotes anchorage-independent growth.

Increasing O-GlcNAcylation Contributes to High-Glucose-Induced Effects in Pancreatic Cells

To understand how high-glucose treatment leads to the reduction of dNTP pools in pancreatic cells, we compared the profiles of glucose-derived metabolites involved in the glycolytic pathway among HPDE, HPNE, and MCF10A cells under high-glucose treatment by mass spectrometry. The levels of glucose-6-phosphate (G6P), fructose-6-phosphate (F6P), and fructose-1,6-bisphosphate (F1,6-BP) were significantly increased in HPDE and HPNE cells but not in MCF10A cells (Figure S4A). In contrast, the metabolite levels of the citric acid cycle did not change significantly (Figure S4B). The increase of F6P in high-glucose-treated pancreatic cells may enhance the hexosamine biosynthetic pathway (HBP) to synthesize uridine diphosphate-N-acetylglucosamine (UDP-GlcNAc), which is the substrate of O-glycosyltransferase (OGT) to catalyze O-GlcNAcylation of target proteins (Yang and Qian, 2017). To address this possibility, we measured the level of UDP-GlcNAc among these cell lines by liquid chromatography-tandem mass spectrometry (LC-MS/MS) analysis and found that HPDE, HPNE, and mouse primary acinar cells, but not other types of cells, contained higher levels of UDP-GlcNAc under high-glucose treatment (Figure 4A, S4C, and S4E). Consistently, the level of global protein O-GlcNAcylation in HPDE, HPNE, and mouse primary acinar cells was also significantly increased but again not in the other cell types (Figures 4B, S4D, and S4E). Similarly, this observation was further confirmed in the sections of pancreatic tissues from tumor-free regions of PDAC patients

(B) The average of single-nucleotide variants in the *Kras* gene in small intestinal tissues and pancreatic tissues collected from mice fed the chow diet or the HS/HF diet. Each group contained 6 mice, and each dot represents the datum from one mouse.

(C and D) The average of single nucleotide variants in the *KRAS* gene in non-tumorigenic human cells (C) and mouse primary acinar cells (D) treated with the indicated concentration of glucose for designated days. n = 3 for each group.

(E) Quantification of KRAS^{G12D}-positive signals by immunofluorescence staining in HPDE, HPNE, MCF10A, H184B4F5/M10, and HS68 cells cultured with the indicated concentrations of glucose for 9, 18, or 27 days. n = 4 for each group.

(F) Quantification of KRAS^{G12D}-positive signals by immunofluorescence staining in mouse primary acinar cells cultured with the indicated concentrations of glucose for 12 days. n = 4 for each group.

(G–J) Colonies of HPDE cells were formed on coverslips after being continually treated with the indicated concentrations of glucose for 12 days and subjected to immunofluorescence staining with KRAS^{G12D} antibody. (G) Representative images of KRAS^{G12D} in a single colony. KRAS^{G12D}, green; DAPI, blue. Scale bar, 50 μm. (H) Quantification of positive and negative colony numbers with or without KRAS^{G12D}-positive cells. (I) The frequency of *de novo* KRAS^{G12D}-posivtive cells. (J) After being continually cultured with 5.5 or 22 mM glucose for 12 days, 1 × 10^6 HPDE cells were subjected to intracellular KRAS^{G12D} staining, cell sorting, single cell PCR with *KRAS* exon 2 primers, and Sanger sequencing.

(K–N) Representative images and quantification of soft agar colony formation of HPDE (K and L) and HPNE (M and N) cells cultured with the indicated concentrations of glucose for 27 days. Each experiment was performed individually 4 times. Scale bar, 50 μm.

(O) Cells were recovered from the soft agar as shown in (K–N) and subjected to genomic DNA extraction, PCR with *KRAS* exon 2 primers, and Sanger sequencing. All values show mean ± SD. *p < 0.05, **p < 0.01, ***p < 0.001 (two-tailed Student's t test).
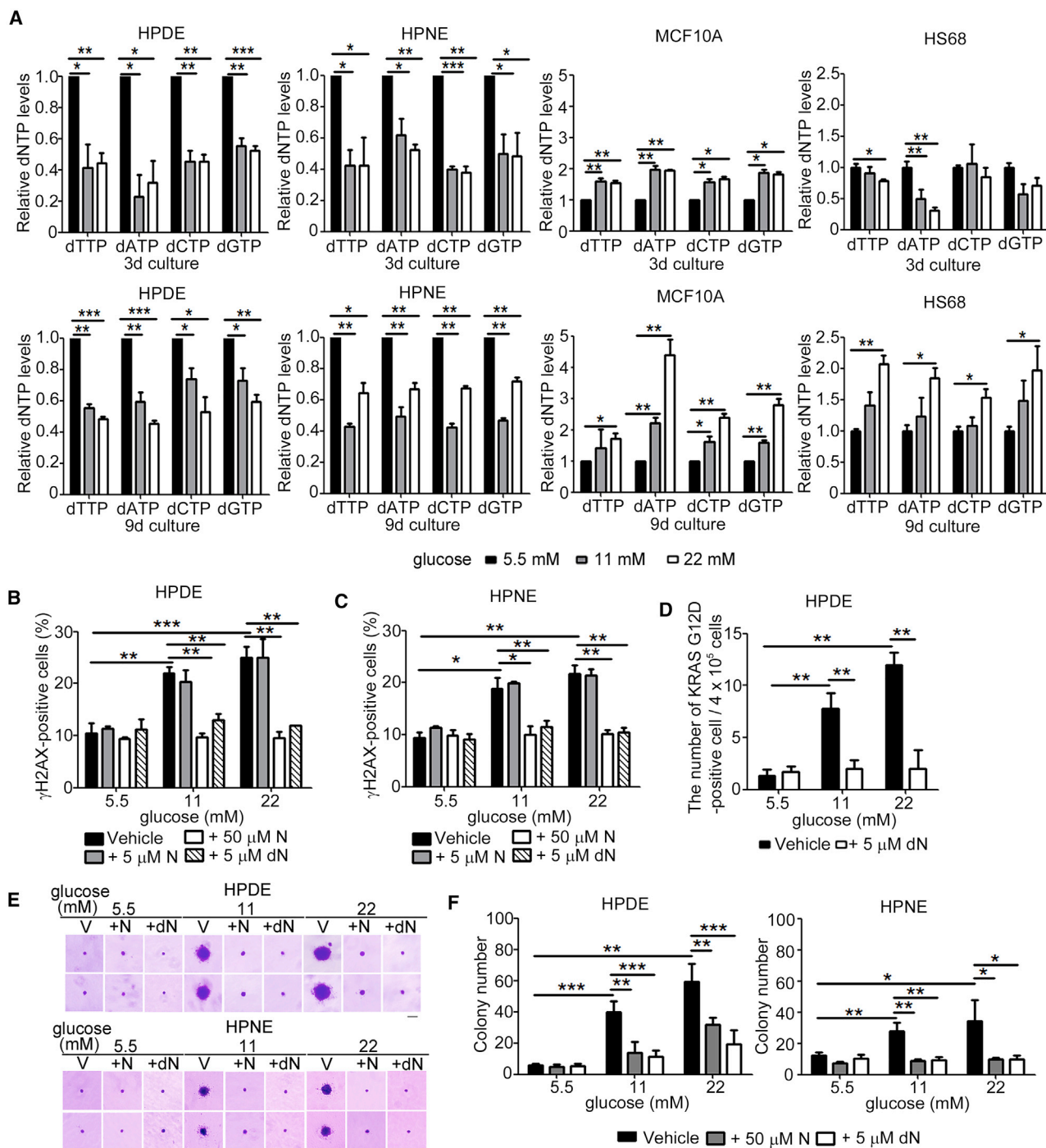
See also Figure S2.

Figure 3. Reduction of the dNTP Pools Increases DNA Damage, Induces Oncogenic *KRAS*[G12D] Mutation, and Enhances Anchorage-Independent Growth in High-Glucose-Treated Pancreatic Cells

(A) Relative levels of dNTPs in cells cultured with the indicated concentrations of glucose for 3 or 9 days. The level of each dNTP was normalized to that from cells cultured with 5.5 mM glucose. Values show mean ± SD (n = 3).

(B and C) Quantification of γH2AX by IF staining in HPDE (B) and HPNE (C) cells cultured with the indicated concentrations of glucose alone, glucose with four ribonucleosides (N), or glucose with four deoxynucleosides (dN) for 3 days. 2,000 cells were counted in each experiment. Values show mean ± SD (n = 4).

(D) Quantification of KRAS[G12D]-positive signals by IF staining in HPDE cells cultured with the indicated concentrations of glucose in the presence or absence of 5 μM dN. Values show mean ± SD (n = 4).

(E and F) Representative images (E) and quantification (F) of the effect of N and dN supply on colony-forming ability of HPDE and HPNE cells cultured with the indicated concentrations of glucose for 27 days. Scale bar, 50 μm. Values show mean ± SD (n = 4). *p < 0.05, **p < 0.01, ***p < 0.001, (two-tailed Student's t test). See also Figure S3.
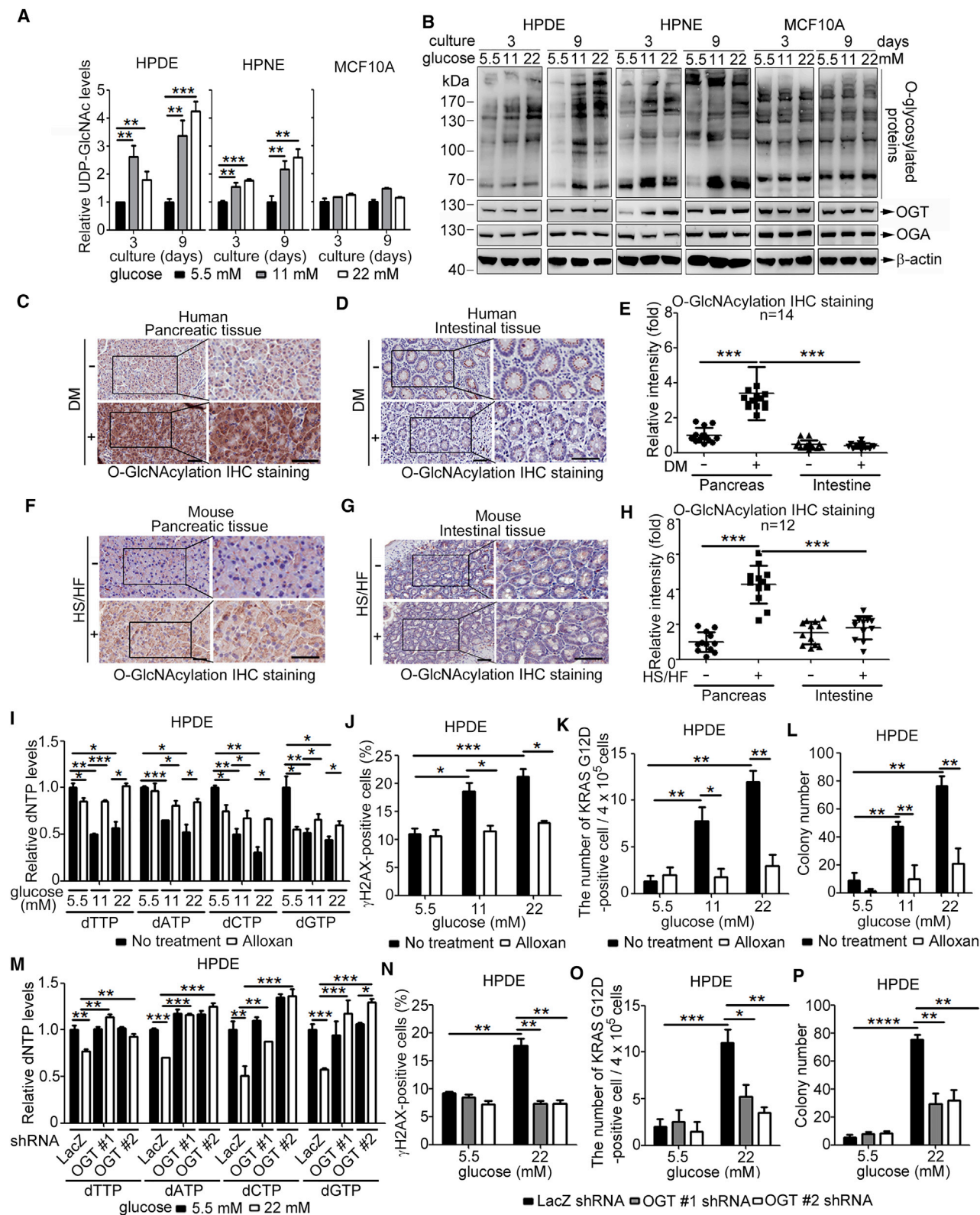
Figure 4. High-Glucose-Induced Effects in Pancreatic Cells Exert through Elevated O-GlcNAcylation

(A and B) Total metabolites were extracted for UDP-GlcNAc determination by LC-MS/MS (A) and total protein was extracted for global O-linked glycosylation measurement by western blot analysis with anti-O-linked N-acetylglucosamine antibody [RL2] (B) from HPDE, HPNE, and MCF10A cells cultured with the

(legend continued on next page)

with DM (Figures 4C–4E) and from male mice fed a HS/HF diet (Figures 4F–4H and S4F–S4H). To test whether O-GlcNAcylation of proteins in pancreatic cells is important for high-glucose-induced phenotypes, we measured the levels of each dNTP pool in HPDE, HPNE, and mouse primary acinar cells after treating with alloxan to inhibit OGT, the critical enzyme responsible for O-GlcNAcylation, and found that the deficiency of dNTP pools was rescued. Furthermore, the level of DNA damage was diminished, the number of KRAS[G12D]-positive cells was decreased, and the colony number of anchorage-independent growth was reduced (Figures 4I–4L and S4I–S4M). Consistently, depletion of OGT by shRNA also subdued high-glucose-induced effects in HPDE cells (Figures 4M–4P and S4N). Similarly, we depleted fructose-6-phosphate amidotransferase-1 (GFAT1), the first and rate-limiting enzyme of the HBP, by lentiviral shRNA, and found that GFAT1 knockdown in HPDE cells diminished high-glucose-induced DNA damage and anchorage-independent growth (Figures S4O–S4Q). Conversely, when pancreatic HPDE and HPNE cells and mammary epithelial MCF10A cells were cultured in the media supplemented with exogenous N-Acetyl-glucosamine, their global protein O-GlcNAcylation and DNA damages were all increased (Figures S4R and S4S). However, only pancreatic cells but not mammary epithelial cells increased KRAS[G12D] mutation (Figures S4T and S4U). Taken together, these results suggest that elevation of O-GlcNAcylation mediates the high-glucose-induced effects preferentially in pancreatic cells.

O-GlcNAcylation of RRM1 at T734 Compromises Ribonucleotide Reductase Enzymatic Activity Contributing to High-Glucose-Induced Effects

Based on the above findings that either adding deoxynucleosides or inhibiting O-GlcNAcylation diminished the high-glucose-induced effects in pancreatic cells (Figures 3 and 4), it is likely that perturbation of the dNTP pools through O-GlcNAcylation of certain key enzymes may be responsible for the observed phenotypes. Ribonucleotide reductase (RNR) and nucleotide diphosphate kinase (NDPK) are two critical enzymes that balance the supply of dNTPs for DNA synthesis and repair. RNR is a tetrameric complex composed of two pairs of RRM1 and RRM2 or

RRM2B subunits and is responsible for the conversion of NDPs (ADP, UDP, CDP, and GDP) to their corresponding dNDPs (Nordlund and Reichard, 2006). On the other hand, NDPK works as a homo-hexamer to synthesize dNTPs through phosphorylation of dNDPs (Lascu and Gonin, 2000). We examined whether RNR or NDPK is affected by high-glucose treatment. Intriguingly, we found that high-glucose treatment reduced the activity of RNR, but not NDPK, in HPDE and HPNE cells (Figures 5A, 5B, S5A, and S5B). To confirm that the decreased activity of RNR was due to hyper-O-GlcNAcylation, we used the OGT inhibitor alloxan to inhibit O-GlcNAcylation and found that the activity of RNR under high-glucose treatment in HPDE and HPNE cells was efficiently rescued, while NDPK activity was not affected (Figures 5A and 5B). Consistently, depletion of OGT with shRNA restored RNR activity under high-glucose-treated conditions (Figure 5C). These results imply that O-GlcNAcylation may regulate RNR activity. Since no significant difference was observed at the level of RNR protein or NADPH (the RNR cofactor) after high-glucose treatment (Figures S5C–S5E), it is likely that hyper-O-GlcNAcylation may disrupt the RNR complex and contribute to the reduction of RNR activity. To explore this possibility, we ectopically expressed RRM1 alone, RRM1 with RRM2, or RRM1 with RRM2B in HEK293T cells and treated these cells with Thiamet G, an O-GlcNAcase (OGA) inhibitor, to enhance O-GlcNAcylation (Figure S5F) and then performed immunoprecipitation. Under normal conditions, RRM1 bound to RRM2 or RRM2B to form a stable complex, while in the presence of Thiamet G, the binding affinity of RRM1 for RRM2 or RRM2B was significantly reduced (Figures 5D and 5E), suggesting that hyper-O-GlcNAcylation induced RNR complex instability. To examine which subunit of RNR is O-GlcNAcylated and therefore presumably affects RNR complex stability, we expressed His-tagged RRM1, RRM2, or RRM2B in an engineered GST-OGT-producing bacterial strain. His-tagged proteins were purified by Ni-NTA agarose and subjected to western blotting analysis with anti-O-GlcNAc antibody. Interestingly, among these subunits of RNR, only RRM1 was O-GlcNAcylated in the engineered GST-OGT-WT-producing bacterial strain but not in the engineered GST-OGT-H568A (a catalytically inactive OGT mutant)-producing bacterial strain (Figure 5F). Moreover,

indicated concentrations of glucose for 3 or 9 days. Levels of UDP-GlcNAc were normalized to those from cells cultured with 5.5 mM glucose. Values show mean ± SD (n = 3).

(C–E) Representative images (C and D) and quantification of O-GlcNAcylation (E) by IHC staining with anti-O-linked N-acetylglucosamine antibody [CTD 110.6] in pancreatic tissues (C) (n = 14) and small intestinal tissues (D) (n = 14) collected from PDAC patients with or without long-standing DM. Each dot represents the datum from one patient. Scale bar, 50 μm. Values show mean ± SD. Levels of O-GlcNAcylation were normalized to those from pancreatic tissues of non-DM patients.

(F–H) Representative images (F and G) and quantification of O-GlcNAcylation (H) by IHC staining with [CTD 110.6] antibody in pancreatic tissues (F) and small intestinal tissues (G) collected from mice fed the chow diet or the HS/HF diet for 20 weeks. Each group contained 12 mice, and each dot represents the datum from one mouse. Scale bar, 50 μm. Values show mean ± SD. Levels of O-GlcNAcylation from mouse tissues were subtracted from the background signal of secondary antibody staining and then normalized to those from pancreatic tissues of mice fed the chow diet.

(I) Relative dNTP levels in HPDE cells after 3-day culture with the indicated concentrations of glucose alone or glucose with 1 mM of alloxan (an OGT inhibitor). Levels of dNTPs were normalized to those from cells cultured with 5.5 mM glucose. Values show mean ± SD (n = 3).

(J) Quantification of γH2AX by immunofluorescence staining in HPDE cells after 3-day culture with the indicated concentrations of glucose alone or glucose with 1 mM of alloxan. 2,000 cells were counted in each experiment. Values show mean ± SD (n = 4).

(K) Quantification of KRAS[G12D]-positive signals by IF staining in HPDE cells cultured with the indicated concentrations of glucose in the presence or absence of 1 mM alloxan for 18 days. Values show mean ± SD (n = 4).

(L) Quantification of soft agar colony formation of HPDE cells after 27-day culture with the indicated concentrations of glucose alone or glucose with 1 mM of alloxan.

(M–P) HPDE cells stably expressing lentiviral LacZ[shRNA] or OGT[shRNA] were subjected to dNTP determination (M), γH2AX measurement (N), KRAS[G12D] staining (O), and soft agar colony formation (P) as described above. Values show mean ± SD (n = 4). *p < 0.05, **p < 0.01, ***p < 0.001 (two-tailed Student's t test).

See also Figure S4.
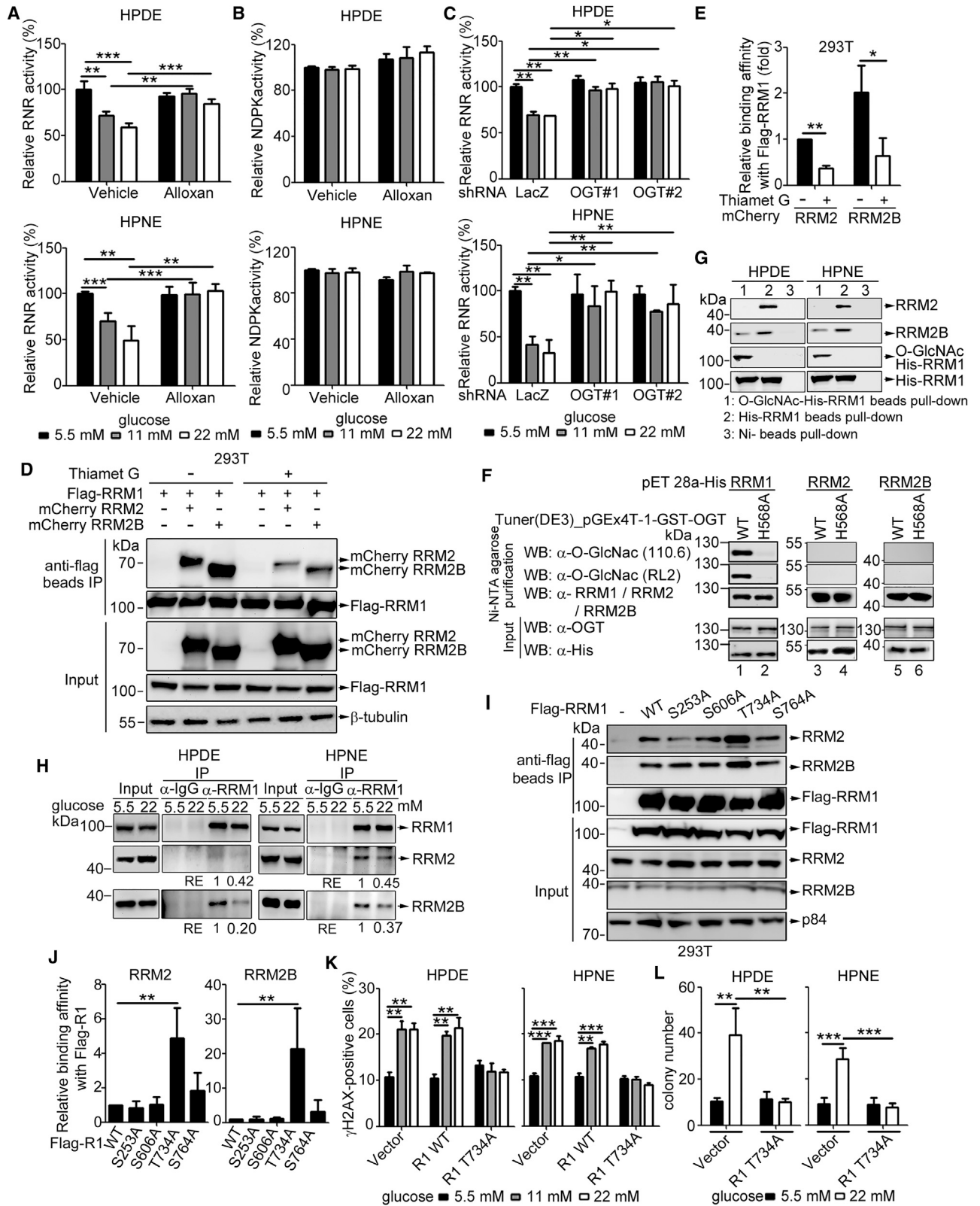
(legend on next page)

hyper-O-GlcNAcylation of RRM1 was also detected in pancreatic tissues but not in small intestinal tissues from mice fed the HS/HF diet (Figure S5G). These data suggest that RRM1 is the major subunit of the RNR complex modified with O-GlcNAcylation. Next, we tested whether O-GlcNAcylation of RRM1 affects the interaction with endogenous RRM2 or RRM2B by performing a pull-down assay with Ni-NTA beads bound to glycosylated or unglycosylated His-RRM1 purified from bacteria. As shown in Figure 5G, glycosylated RRM1 showed reduced binding activity to RRM2 and RRM2B, while unglycosylated RRM1 formed a stable complex. To confirm this observation, we performed immunoprecipitation with succinylated wheat germ agglutinin (sWGA) beads to pull down endogenous glycosylated proteins in HPDE and HPNE cells. The endogenous RRM1 was highly glycosylated under high-glucose treatment (Figure S5H) and formed a less stable RNR complex (Figure 5H), suggesting that O-GlcNAcylation of RRM1 disrupts the RNR complex in high-glucose-treated pancreatic cells.

To further pinpoint how O-GlcNAcylation affects RRM1 activity, we performed liquid chromatography-tandem mass spectrometry (LC-MS/MS) analysis of glycosylated recombinant RRM1 and found four highly confident sites: S253, S606, T734, and S764 of RRM1 (Figure S5I). To examine which site affects RNR complex formation, we generated S253, S606, T734, and S764 mutants for co-immunoprecipitation analysis and identified that T734 was critical for RNR complex formation (Figures 5I and 5J). Furthermore, when we ectopically expressed RRM1-T734A in HPDE and HPNE cells, these cells no longer had high-glucose-induced effects (Figures 5K, 5L, and S5J). Taken together, these results suggest that high-glucose-induced DNA damage and anchorage-independent growth in pancreatic cells are mediated by O-GlcNAcylation of RRM1 at its T734 site, which destabilizes the formation of a functional RNR complex.

Reduction in Phosphofructokinase Activity Renders Pancreatic Cells Sensitive to High Glucose

Next, we addressed why the high glucose-induced effect preferentially occurred in pancreatic cells. The high steady-state levels of G6P, F6P, and F1,6-BP in pancreatic cells (Figure 6A) suggested that the activity of glucose-6-phosphate dehydrogenase (G6PD), which converts G6P into 6-phosphoglucono-δ-lactone and NADP$^+$ to NADPH; the activity of aldolase, which catalyzes the reversible conversion of F1,6-BP to glyceraldehyde 3-phosphate and dihydroxyacetone phosphate; or the activity of phosphofructokinase (PFK), which catalyzes the committed step converting F6P to F1,6-BP and ATP to ADP, may differ in these cells. Through enzymatic activity assays, we found that PFK activity of HPDE and HPNE cells was three times lower than that of MCF10A cells (Figure 6B), but G6PD and aldolase activity showed no difference among these cells (Figures S6A–S6D). Consistently, the mRNA and protein levels of PFK isoforms (L, M, and P) were lower in HPDE and HPNE than in MCF10A cells (Figures 6C–6E). Similarly, lower levels of PFK mRNA and protein in mouse pancreatic tissue were also observed when compared with other tissues (Figures S6E–S6G). Furthermore, overall PFK activity was further reduced in HPDE and HPNE cells under high-glucose conditions, and increasing O-GlcNAcylation of each PFK isoform was detected (Figures 6F and 6G). To confirm the importance of PFK activity in pancreatic cells, we overexpressed PFKL or PFKM in HPDE and HPNE cells and found that the cells with enhanced PFK activity resisted the high-glucose-induced effects (Figures 6H and 6L). In contrast, depletion of PFKL, the major form of PFK (Moon et al., 2011) in MCF10A cells, conferred high-glucose-induced effects on these cells (Figures 6M–6R). These results indicate that the reduction of PFK activity that alters the glucose metabolic pathway contributes to the high-glucose-induced effects in pancreatic cells.

We also examined the transporters responsible for glucose uptake, including GLUTs and SGLTs, and found that they were expressed similarly in all types of cells, but the level of the active form (membrane form) of the glucose transporters was higher in pancreatic cells, which is consistent with their slightly higher glucose uptake efficiency than other types of cells (Figures S6H–S6K). Although inhibiting these glucose transporters in pancreatic cells decreased glucose uptake and abolished high-glucose-induced DNA damage (Figures S6L and S6M),

---

Figure 5. O-GlcNAcylation of RRM1 at T734 Disrupts the RNR Complex, Reduces RNR Activity, and Leads to High-Glucose-Induced Effects in Pancreatic Cells

(A and B) Relative activity of RNR (A) and NDPK (B) in HPDE and HPNE cells cultured with the indicated concentrations of glucose with vehicle control or with 1 mM alloxan for 3 days. Values show mean ± SD (n = 3).

(C) Relative activity of RNR in HPDE and HPNE cells stably expressing LacZ^{shRNA} or OGT^{shRNA} cultured with the indicated concentrations of glucose for 3 days. Values show mean ± SD (n = 3).

(D and E) HEK293T cells were transfected with FLAG-RRM1 in the presence or absence of mCherry RRM2 or RRM2B as indicated. After overnight incubation with or without thiamet G (an OGA inhibitor), cells were lysed for RNR complex detection by pull-down assay with anti-FLAG beads and western blot with indicated antibodies (D). The relative binding affinity of RRM1 to RRM2 and RRM1 to RRM2B was quantified, respectively (E). Values show mean ± SD (n = 3).

(F) Detection of O-GlcNAcylation catalyzed by OGT on recombinant His-tagged RNR subunits (RRM1, RRM2, or RRM2B) by western blot with anti-O-linked N-acetylglucosamine antibody [CTD 110.6 or RL2]. OGT-H568A is a catalytically inactive mutant.

(G) Effect of glycosylated RRM1 on RNR complex formation was determined by pull-down assay with HPDE or HPNE lysates.

(H) Endogenous RNR complex formation was determined by immunoprecipitation with RRM1 antibody and western blot with the indicated antibodies in HPDE and HPNE cells cultured with 5.5 or 22 mM glucose for 3 days.

(I and J) HEK293T cells were transfected with WT or the indicated mutant form of Flag-RRM1. After overnight incubation of thiamet G, cells were lysed for RNR complex detection by pull-down assay with anti-FLAG beads and western blot with the indicated antibodies (I). The relative binding affinity of RRM1 to RRM2 and RRM2B was quantified (J). Values show mean ± SD (n = 4).

(K) Quantification of γH2AX by IF staining in HPDE cells stably expressing lentiviral vector, RRM1(R1)-WT, or R1-T734A mutant after 3-day culture with the indicated concentrations of glucose. Values show mean ± SD (n = 3).

(L) HPDE and HPNE cells stably expressing lentiviral vector or R1-T734A were subjected to soft agar colony formation assay with the indicated concentrations of glucose for 27 days. Values show mean ± SD (n = 4). *p < 0.05, **p < 0.01, *** p < 0.001 (two-tailed Student's t test).

See also Figure S5.
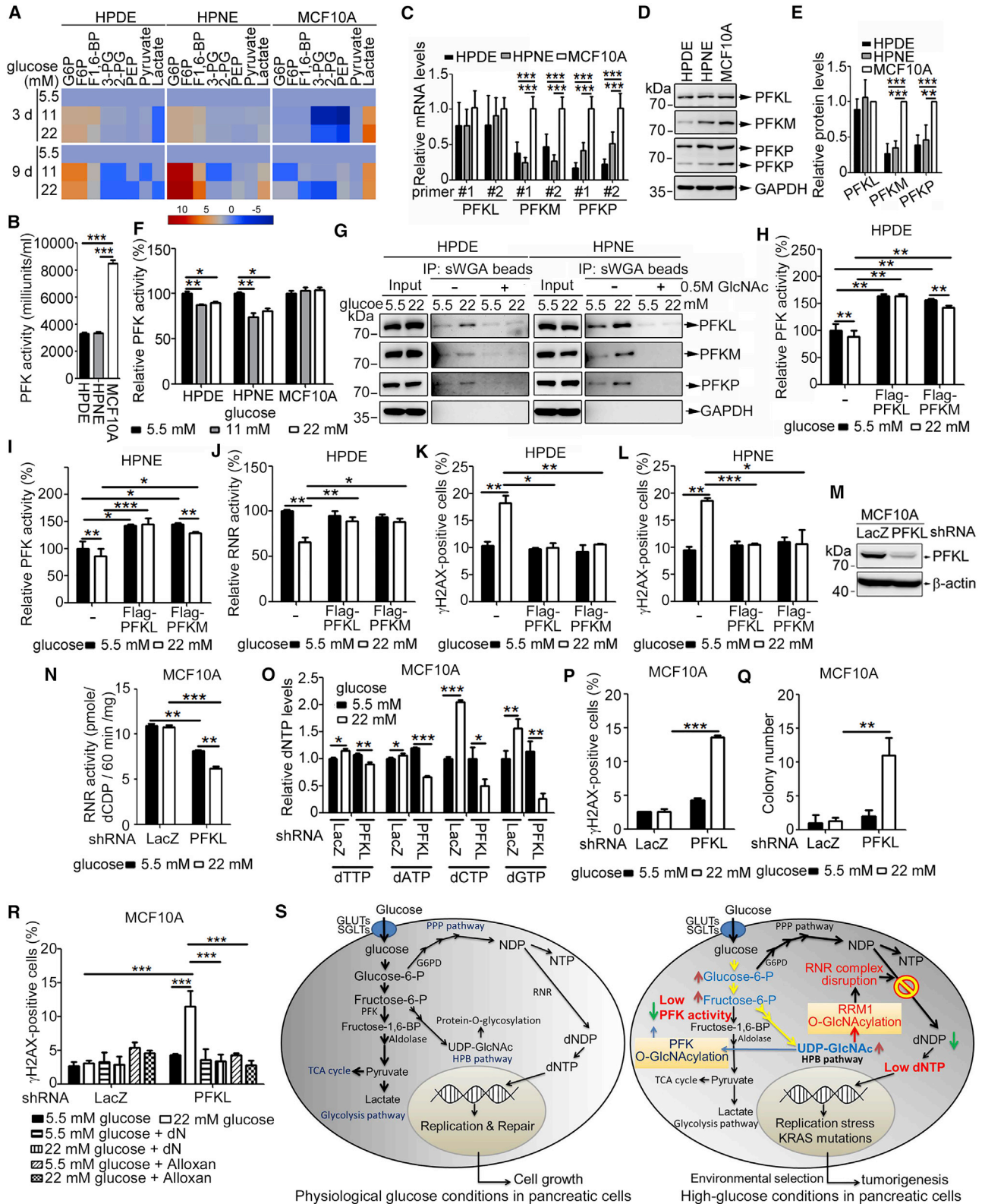
Figure 6. Reduction of Phosphofructokinase Activity Confers the Sensitivity of High-Glucose-Induced Effects in Pancreatic Cells

(A) Heat map of glycolysis metabolites in HPDE, HPNE, and MCF10A cells cultured with the indicated concentrations of glucose for 3 or 9 days. A 10-fold increase in relative amount of metabolites is shown in red and a 5-fold decrease is shown in dark blue.

increasing glucose uptake by overexpressing GLUT1 in MCF10A cells showed no significant effect on high-glucose-induced DNA damage (Figures S6N–S6P), suggesting that the glucose uptake machinery is not fully responsible for the high-glucose-induced effects in pancreatic cells.

Based on the above results, it appears that pancreatic cells uptake more glucose via GLUTs and SGLTs, accumulate higher levels of F6P/G6P because of lower PFK activity, and increase UDP-GlcNAc levels to enhance global O-GlcNAcylation on key enzymes under high-glucose conditions. Glycosylated PFK further reduces its activity, and glycosylated RRM1 compromises complex assembly and reduces RNR activity. This disturbs dNTP pools leading to genomic instability with increasing frequency of *de novo* oncogenic *KRAS* mutation and initiation of tumorigenesis (Figure 6S). These results provide a mechanistic view of how an alteration in sugar metabolism leads to genomic lesions to initiate tumorigenesis in pancreatic cells.

DISCUSSION

High blood glucose is associated with an increased risk of pancreatic cancer across the range of pre-diabetes and diabetes (Liao et al., 2015). It was also noted that the prevalence of diabetes was preferentially high in pancreatic cancer compared with other cancers such as lung, breast, prostate, and colorectal cancer (CRC) (Aggarwal et al., 2013). Intriguingly, there is no report of high blood glucose associated with brain tumors. Since the brain depends on glucose as its main source of energy for neuron survival, neurotransmitter synthesis, and synaptic activity (Mergenthaler et al., 2013) the majority of the glucose is metabolized to pyruvate, which is transported to mitochondria for ATP production (Bélanger et al., 2011). Although diabetes is a risk factor for lung cancer and CRC, only a fraction of cases also harbor *KRAS* mutation. This is consistent with the observation that PFK activity is higher in lung and colon tissues than in pancreatic tissue (Figures S6E–S6G) and high glucose treatment has little impact on these cells (Figures S1P–S1S). This observation implicates that other mechanisms are involved in *KRAS* mutation in lung and colon cells.

Importantly, PFK activity appears to play a key role in determining the utilization of glucose that generates specific metabolites to affect different tissues or cells. Lower expression of PFK isoforms in pancreatic cells contributed to its lower PFK activity

(Figures 6B–6E), and an increase of PFK activity in pancreatic cells decreased the number of high-glucose-induced DNA damage (Figures 6H–6L). With high-glucose treatment, more glucose metabolites entered the HBP to increase UDP-GlcNAc levels for O-GlcNAcylation in pancreatic cells. This is distinct from more glucose consumption via the glycolytic pathway as indicated by high lactate accumulation in other cell types (Figures 4A, 4B, S4A, S4B, S4C, and S4D). Elevation of O-GlcNAcylation mediated the high-glucose-induced effects in pancreatic cells (Figure 4). This notion was further supported by the results demonstrating that depletion of GFAT1, the first and rate-limiting enzyme of the HBP, diminished high-glucose-induced DNA damage and anchorage-independent growth in pancreatic cells (Figures S4O–S4Q). Conversely, supplementing the media with exogenous N-Acetyl-glucosamine increased global protein O-GlcNAcylation and DNA damage in pancreatic cells (Figures S4R and S4S). Taking these results together, it suggested that the reduction of PFK activity rewires the glucose metabolic pathway to favor O-GlcNAcylation pathway, contributing to the high-glucose-induced effects in pancreatic cells. Although it is well documented that during development process, epigenetic regulation of gene expression occurs in different tissues and cell types (Lokk et al., 2014), why pancreatic cells express low PFK activity and favor the HBP under high-glucose condition warrants further investigation.

Cellular O-GlcNAcylation homeostasis is achieved through coordinating the optimal levels of substrate UDP-GlcNAc and the O-GlcNAc-cycling enzymes, OGT and OGA (Yang and Qian, 2017). Abnormal O-GlcNAcylation is increasingly recognized as a general characteristic of cancer cells (de Queiroz et al., 2014; Qian et al., 2018). The recent studies suggested that O-GlcNAcylation is a key communicator of nutritional status to regulate critical signaling and metabolic pathways (Bond and Hanover, 2015; Ma and Vosseller, 2014; Yang and Qian, 2017). In this study, we found that high-glucose treatment significantly elevated cellular levels of UDP-GlcNAc and O-GlcNAcylation but had little effect on OGT and OGA protein expression in normal pancreatic cells (Figures 4A and 4B), indicating that metabolite imbalance is the key factor to increase of O-GlcNAcylation in pancreatic cells. Furthermore, either DM or the HS/HF diet increased O-GlcNAcylation only in pancreatic tissues (Figures 4C–4H, S4F, and S4H) and that pancreatic cells growing in a high-glucose setting increased O-GlcNAcylation

(B) Measurement of PFK activity in cells under 5.5 mM glucose conditions.

(C–E) mRNA (C) and representative images (D) and quantification (E) of protein levels of PFK isoforms (L, M, and P) in cells under 5.5 mM glucose conditions. Values show mean ± SD (n = 4). mRNA and protein levels of each PFK isoform were normalized to those from MCF10A cells. GAPDH serves as an internal control.

(F) Relative activity of PFK in HPDE, HPNE, and MCF10A cells cultured with the indicated concentrations of glucose for 3 days. The enzyme activity in cells cultured with 5.5 mM glucose is set as 100%. Values show mean ± SD (n = 3).

(G) Detection of O-GlcNAc-modified PFK by succinylated wheat germ agglutinin (sWGA)-immunoprecipitation in HPDE and HPNE cells cultured with 5.5 or 22 mM glucose for 3 days. Addition of 0.5 M GlcNAc serves as a negative control.

(H–L) Relative PFK activity (H and I), relative RNR activity (J), and γH2AX measurement (K and L) in HPDE and HPNE cells infected with the retrovirus that carries FLAG-PFKL or FLAG-PFKM and then cultured with 5.5 or 22 mM glucose for 3 days.

(M–R) MCF10A cells stably expressing lentiviral LacZ[shRNA] or PFKL[shRNA] were subjected to western blot analysis (M), RNR activity (N), dNTP pool determination (O), and γH2AX measurement (P) after 3-day culture with the indicated concentrations of glucose. Values show mean ± SD (n = 3). (Q) Quantification of soft agar colony formation of MCF10A cells after 27-day culture with the indicated concentrations of glucose. Values show mean ± SD (n = 4). (R) γH2AX measurement of MCF10A cells after 3-day culture with the indicated concentrations of glucose alone, glucose with 5 μM dN or glucose with 1 mM alloxan. Values show mean ± SD (n = 3).

(S) Proposed model of high-glucose-treatment-induced *KRAS* mutations in pancreatic cells. For quantification of γH2AX-positive cells, 2,000 cells were counted in each experiment. *p < 0.05, **p < 0.01, ***p < 0.001 (two-tailed Student's t test). See also Figure S6.

(Figures 4B and S4E) support this notion (de Queiroz et al., 2014). Interestingly, RRM1, the large subunit of RNR, was hyper-O-GlcNAcylated, and the enzymatic activity of RNR was reduced under high-glucose treatment in pancreatic cells (Figure 5). Compromising this key step of dNTP synthesis led to an imbalance of dNTP pools and accelerated mutagenesis, likely through replication stress, resulting in cancer development (Mathews, 2015). This novel modulation of RNR activity through O-GlcNAcylation of RRM1 at T734 links glucose and nucleotide metabolism in cancer initiation. Interestingly, it was reported that O-GlcNAcylation of oncogenic transcription factor Sox2 in pancreatic cancer cells is responsible for tumor initiation (Nikita Sharma et al., 2018; Qian et al., 2018). It would be worthwhile to investigate whether O-GlcNAcylation of RRM1, similar to Sox2, has a significant impact on cancer initiation and progression in general.

Reduction of the dNTP pools in pancreatic cells treated with high glucose increased DNA damage and genomic instability. The average of SNVs in *KRAS*, but not in *GAPDH*, was significantly higher in pancreatic tissue of PDAC patients with DM than without DM and higher than that in small intestinal tissue of PDAC patients with/without DM (Figures 2A and S2A–S2C). Similarly, the average of SNVs in *Kras*, but not in *Gapdh*, was significantly higher in pancreatic tissue from mice fed the HS/HF diet than in small intestinal tissue from mice fed the same diet as well as higher than that noted in pancreas and intestine from mice fed the chow diet (Figures 2B, S2E, and S2F). Consistently, high-glucose treatment could preferentially increase *Kras* mutations in mouse primary pancreatic cells (Figures 2C, 2D, and S2G–S2L). However, no obvious nucleotide mutational signature was found under these conditions. Furthermore, either high glucose or addition of N-Acetylglucosamine preferentially increased the oncogenic KRAS^{G12D} mutation in pancreatic cells, indicating mutation rate of a given gene may be cell type dependent (Figures 2E, S4T, and S4U). It was reported that context-specific differences in chromatin organization (Schuster-Böckler and Lehner, 2012), G+C content (Gojobori et al., 1982), CpG dinucleotide frequency (Hwang and Green, 2004), replicating time (Stamatoyannopoulos et al., 2009), nucleosome binding (Chen et al., 2012), and epigenomic profiles (Cramer et al., 2016; Polak et al., 2015) determined the rate of somatic mutations across the genome of different cell types. In addition, transcription-associated mutation, transcription-coupled repair, and replication-transcription collisions also play a key role in determining the mutation rate of a given gene (Hanawalt and Spivak, 2008; Kim and Jinks-Robertson, 2012). Given that reducing O-GlcNAcylation eliminated the high-glucose-induced genomic alterations (Figures 4J, 4K, 4N, 4O, S4J, and S4L), it is foreseeable that elevated O-GlcNAcylation of factors participating in these processes may contribute to the preferential increase in the mutation rate of the *KRAS* gene in pancreatic cells.

Why is the *KRAS* mutation preferentially high in PDAC? We may explain this phenotype with two steps; the first is that high glucose triggers genomic alterations including *KRAS* mutation in pancreatic cells. The second is that the cells with the oncogenic *KRAS* mutation must have the advantage to develop pancreatic intraepithelial neoplasia (PanIN) and PDAC. Clearly, high glucose triggers a metabolic imbalance leading to genomic mutations,

including in the *KRAS* gene with the oncogenic *KRAS* mutation, in pancreatic cells (Figures 2 and S2). Cells with the oncogenic *Kras* mutation have growth advantage under high-and normal-glucose conditions compared to cells with wild-type *Kras* (Figure S2P). In addition, oncogenic *KRAS* has been implicated in reprogramming glucose, glutamine, and nucleotide metabolism to support rapid proliferation of cancer cells (Bryant et al., 2014; Ying et al., 2012). Thus, cells with oncogenic *KRAS* have a growth advantage for clonal selection. Besides metabolic reprogramming, PDAC is also characterized by abundant extracellular matrix, vasculature, and a distinct stromal component with increased numbers of pancreatic stellate cells, activated fibroblasts, pro-inflammatory macrophages, immunosuppressive myeloid cells, and immunosuppressive lymphoid cells. This stromal milieu contributes to the survival and progression of the disease (Collins et al., 2012; Pylayeva-Gupta et al., 2011; Tape et al., 2016; Wu et al., 2015), indicating that a reciprocal interaction between the *KRAS*-mutated pancreatic cells and the surrounding microenvironment must provide a positive selection force for maintaining the mutated *KRAS* in PDAC. How this selection proceeds is a compelling direction for future investigation.

Limitation of the Study

The reads for each nucleotide in whole genome sequencing are about 30-100 coverage. This level of reads is not sufficiently sensitive for detecting SNVs in a whole genome scale of few cells out of millions in population. Although NGS provides a suitable platform for detecting minor variants within heterogeneous mixtures, low-frequency variants (VAF $\leq$ 5%) are often confounded by sequencing errors that exist at a rate of 0.01–0.1 per base on library preparation involving PCR, sequencing, and base calling (Kinde et al., 2011; Lou et al., 2013; Schirmer et al., 2015). A sensitive methodology remains to be established for determining mutation rate in an accurate manner. To circumvent this technical challenge, we focused on several selected genes including *KRAS* in this study. However, it will be the best to compare whole genome alterations without individual gene bias.

It was also noted that 87% of the oncogenic KRAS mutations in PDAC patients are at amino acid G12 and 41% of those are G12D. However, only a specific antibody recognizing KRAS^{G12D} is available for confirming the presence of the oncogenic KRAS^{G12D} mutation. Thus, either NGS or immunostaining with a specific KRAS^{G12D} antibody has its detection limitation. The measurement described herein should be considered as semi-quantitative. Further improvement for accurate determination of mutation frequency is clearly needed.

High glucose induces *KRAS* mutation in pancreatic cells is clearly described herein. However, how this mutation is actually generated in pancreatic cells during human or mouse lifespan remains to be explored. There is a great portion of PDAC patients without DM, suggesting that long-term hyperglycemia is not essential for PDAC. However, it is likely that pancreatic cells in animals are susceptible to high glucose-induced mutation under certain situations. Since *KRAS* mutation alone is not sufficient to generate PDAC (Aguirre et al., 2003; Chang et al., 2013; Hingorani et al., 2003), pancreatic cells containing *KRAS* mutation may have subtle phenotypic change at the beginning. It will be difficult to pinpoint which cells already had the *KRAS* mutation under high

glucose treatment. Thus, it is essential to improve the current detection method for further addressing this type of questions.

STAR★METHODS

Detailed methods are provided in the online version of this paper and include the following:

- KEY RESOURCES TABLE
- CONTACT FOR REAGENT AND RESOURCE SHARING
- EXPERIMENTAL MODEL AND SUBJECT DETAIL
  - Ethics Statement
  - Human Specimens
  - Animal Protocols, Diets, and Treatment
  - Sample Size Estimation
  - General Cell Culture and Establishment of Stable Cell Lines
  - Mouse Primary Pancreatic Acinar Cell Culture
- METHODS DETAILS
  - Plasmids, Construction of Expression Plasmids, and Site-Directed Mutagenesis
  - Immunohistochemistry (IHC)
  - Immunofluorescence Staining
  - Soft Agar Colony Formation Assay
  - Glucose Metabolite Analysis
  - Cellular dNTP Extraction and Quantification
  - Analysis of UDP-GlcNAC Using Liquid Chromatography-Mass Spectrometry (LC-MS)
  - Cellular RNR Activity Analysis
  - NDPK Activity Analysis
  - PFK Activity Measurement
  - sWGA Pull-Down Assay
  - Immunoprecipitation and Immunoblotting
  - Protein Purification
  - Protein In Vitro Binding Assay
  - Genomic DNA Extraction
  - Amplicon Library Preparation
  - Sequencing with Illumina MiSeq and Data Analysis
  - Lentiviral shRNA, Lentiviral cDNA, and Retroviral cDNA Production for Infection
  - Cell Growth, Cell Cycle, and 2D Clonogenic Cell Survival Analysis
  - Protein Extraction and Western Blotting Analysis
  - Cellular ROS Measurement
  - Analysis of NTPs Using Liquid Chromatography-Mass Spectrometry (LC-MS)
  - Cellular NADPH Measurement
  - G6PDH and Aldolase Activity Measurement
  - Glucose Uptake Assay
  - Flow Cytometry for Cell Cycle Analysis
  - Flow Cytometry for KRAS^{G12D} Analysis
  - Flow Cytometry for Glucose Uptake Analysis
  - In-Gel Digestion of Purified RRM1 Protein
  - LC-MS/MS Analysis
  - Data Processing and Database Search
  - Experiment Design
- QUANTIFICATION AND STATISTICAL ANALYSIS
  - Statistical Analyses
- DATA AND SOFTWARE AVAILABILITY

SUPPLEMENTAL INFORMATION

Supplemental Information can be found with this article online at https://doi.org/10.1016/j.cmet.2019.02.005.

AUTHOR CONTRIBUTIONS

C.-M.H. designed and performed the experiments and analyzed the data. S.-C.T. performed the O-GlcNAcylation of RNR experiments and determined the expression levels of glucose transporters in various cells. Y.-M.J. analyzed the immunohistochemistry data. M.-C.C. and Y.-T.C. provided clinical samples. Yi-Ju C. and Yu-Ju C. performed the MS analysis for identifying the potential O-GlcNAcylation sites of RRM1. C.-M.H., P.-K.H., E.Y.-H.P.L., and W.-H.L. composed the manuscript. C.-M.H. and W.-H.L. coordinated and supervised the entire project.

REFERENCES

Aggarwal, G., Kamada, P., and Chari, S.T. (2013). Prevalence of diabetes mellitus in pancreatic cancer compared to common cancers. Pancreas *42*, 198–201.

Aguirre, A.J., Bardeesy, N., Sinha, M., Lopez, L., Tuveson, D.A., Horner, J., Redston, M.S., and DePinho, R.A. (2003). Activated Kras and Ink4a/Arf deficiency cooperate to produce metastatic pancreatic ductal adenocarcinoma. Genes Dev. *17*, 3112–3126.

Bélanger, M., Allaman, I., and Magistretti, P.J. (2011). Brain energy metabolism: focus on astrocyte-neuron metabolic cooperation. Cell Metab. *14*, 724–738.

Biankin, A.V., Waddell, N., Kassahn, K.S., Gingras, M.C., Muthuswamy, L.B., Johns, A.L., Miller, D.K., Wilson, P.J., Patch, A.M., Wu, J., et al. (2012). Pancreatic cancer genomes reveal aberrations in axon guidance pathway genes. Nature *491*, 399–405.

Bond, M.R., and Hanover, J.A. (2015). A little sugar goes a long way: the cell biology of O-GlcNAc. J. Cell Biol. *208*, 869–880.

Bonner, W.M., Redon, C.E., Dickey, J.S., Nakamura, A.J., Sedelnikova, O.A., Solier, S., and Pommier, Y. (2008). GammaH2AX and cancer. Nat. Rev. Cancer *8*, 957–967.

Bryant, K.L., Mancias, J.D., Kimmelman, A.C., and Der, C.J. (2014). KRAS: feeding pancreatic cancer proliferation. Trends Biochem. Sci. *39*, 91–100.

Campbell, P.J., Yachida, S., Mudie, L.J., Stephens, P.J., Pleasance, E.D., Stebbings, L.A., Morsberger, L.A., Latimer, C., McLaren, S., Lin, M.L., et al. (2010). The patterns and dynamics of genomic instability in metastatic pancreatic cancer. Nature *467*, 1109–1113.

Chang, Z., Li, Z., Wang, X., Kang, Y., Yuan, Y., Niu, J., Wang, H., Chatterjee, D., Fleming, J.B., Li, M., et al. (2013). Deciphering the mechanisms of tumorigenesis in human pancreatic ductal epithelial cells. Clin. Cancer Res. 19, 549–559.

Chen, X., Chen, Z., Chen, H., Su, Z., Yang, J., Lin, F., Shi, S., and He, X. (2012). Nucleosomes suppress spontaneous mutations base-specifically in eukaryotes. Science 335, 1235–1238.

Collins, M.A., Bednar, F., Zhang, Y., Brisset, J.C., Galbán, S., Galbán, C.J., Rakshit, S., Flannagan, K.S., Adsay, N.V., and Pasca di Magliano, M. (2012). Oncogenic Kras is required for both the initiation and maintenance of pancreatic cancer in mice. J. Clin. Invest. 122, 639–653.

Cooke, M.S., Evans, M.D., Dizdaroglu, M., and Lunec, J. (2003). Oxidative DNA damage: mechanisms, mutation, and disease. FASEB J. 17, 1195–1214.

Cramer, D., Serrano, L., and Schaefer, M.H. (2016). A network of epigenetic modifiers and DNA repair genes controls tissue-specific copy number alteration preference. Elife 5.

de Queiroz, R.M., Carvalho, E., and Dias, W.B. (2014). O-GlcNAcylation: the sweet side of the cancer. Front. Oncol. 4, 132.

Eser, S., Schnieke, A., Schneider, G., and Saur, D. (2014). Oncogenic KRAS signalling in pancreatic cancer. Br. J. Cancer 111, 817–822.

Ferraro, P., Franzolin, E., Pontarin, G., Reichard, P., and Bianchi, V. (2010). Quantitation of cellular deoxynucleoside triphosphates. Nucleic Acids Res. 38, e85.

Gojobori, T., Li, W.H., and Graur, D. (1982). Patterns of nucleotide substitution in pseudogenes and functional genes. J. Mol. Evol. 18, 360–369.

Gout, J., Pommier, R.M., Vincent, D.F., Kaniewski, B., Martel, S., Valcourt, U., and Bartholin, L. (2013). Isolation and culture of mouse primary pancreatic acinar cells. J. Vis. Exp. https://doi.org/10.3791/50514.

Hanawalt, P.C., and Spivak, G. (2008). Transcription-coupled DNA repair: two decades of progress and surprises. Nat. Rev. Mol. Cell Biol. 9, 958–970.

Hezel, A.F., Kimmelman, A.C., Stanger, B.Z., Bardeesy, N., and Depinho, R.A. (2006). Genetics and biology of pancreatic ductal adenocarcinoma. Genes Dev. 20, 1218–1249.

Hingorani, S.R., Petricoin, E.F., Maitra, A., Rajapakse, V., King, C., Jacobetz, M.A., Ross, S., Conrads, T.P., Veenstra, T.D., Hitt, B.A., et al. (2003). Preinvasive and invasive ductal pancreatic cancer and its early detection in the mouse. Cancer Cell 4, 437–450.

Huang, H., Daniluk, J., Liu, Y., Chu, J., Li, Z., Ji, B., and Logsdon, C.D. (2014). Oncogenic K-Ras requires activation for enhanced activity. Oncogene 33, 532–535.

Hwang, D.G., and Green, P. (2004). Bayesian Markov chain Monte Carlo sequence analysis reveals varying neutral substitution patterns in mammalian evolution. Proc. Natl. Acad. Sci. U S A 101, 13994–14001.

Jena, N.R. (2012). DNA damage by reactive species: mechanisms, mutation and repair. J. Biosci. 37, 503–517.

Jong, A.Y., Yu, K., Zhou, B., Frgala, T., Reynolds, C.P., and Yen, Y. (1998). A simple and sensitive ribonucleotide reductase assay. J. Biomed. Sci. 5, 62–68.

Kim, N., and Jinks-Robertson, S. (2012). Transcription as a source of genome instability. Nat. Rev. Genet. 13, 204–214.

Kinde, I., Wu, J., Papadopoulos, N., Kinzler, K.W., and Vogelstein, B. (2011). Detection and quantification of rare mutations with massively parallel sequencing. Proc. Natl. Acad. Sci. U S A 108, 9530–9535.

Lascu, I., and Gonin, P. (2000). The catalytic mechanism of nucleoside diphosphate kinases. J. Bioenerg. Biomembr. 32, 237–246.

Liao, W.C., Tu, Y.K., Wu, M.S., Lin, J.T., Wang, H.P., and Chien, K.L. (2015). Blood glucose concentration and risk of pancreatic cancer: systematic review and dose-response meta-analysis. BMJ 349, g7371.

Lokk, K., Modhukur, V., Rajashekar, B., Märtens, K., Mägi, R., Kolde, R., Koltšina, M., Nilsson, T.K., Vilo, J., Salumets, A., et al. (2014). DNA methylome profiling of human tissues identifies global and tissue-specific methylation patterns. Genome Biol. 15, r54.

Longnecker, D. (2014) Anatomy and Histology of the Pancreas. Pancreapedia: Exocrine Pancreas Knowledge Base, 1–26.

Lou, D.I., Hussmann, J.A., McBee, R.M., Acevedo, A., Andino, R., Press, W.H., and Sawyer, S.L. (2013). High-throughput DNA sequencing errors are reduced by orders of magnitude using circle sequencing. Proc. Natl. Acad. Sci. U S A 110, 19872–19877.

Ma, Z., and Vosseller, K. (2014). Cancer metabolism and elevated O-GlcNAc in oncogenic signaling. J. Biol. Chem. 289, 34457–34465.

Mathews, C.K. (2015). Deoxyribonucleotide metabolism, mutagenesis and cancer. Nat. Rev. Cancer 15, 528–539.

Mergenthaler, P., Lindauer, U., Dienel, G.A., and Meisel, A. (2013). Sugar for the brain: the role of glucose in physiological and pathological brain function. Trends Neurosci. 36, 587–597.

Moon, J.S., Kim, H.E., Koh, E., Park, S.H., Jin, W.J., Park, B.W., Park, S.W., and Kim, K.S. (2011). Kruppel-like factor 4 (KLF4) activates the transcription of the gene for the platelet isoform of phosphofructokinase (PFKP) in breast cancer. J. Biol. Chem. 286, 23808–23816.

Nikita Sharma, V.K.G., Dauer, P., Kesh, K., Hadad, R., Giri, B., Chandra, A., Dudeja, V., Slawson, C., Banerjee, S., Vickers, S.M., et al. (2018). O-GlcNAc modification of oncogenic transcription factor Sox2 promotes protein stability and regulates self-renewal in pancreatic cancer. bioRxiv. https://doi.org/10.1101/345223.

Nordlund, P., and Reichard, P. (2006). Ribonucleotide reductases. Annu. Rev. Biochem. 75, 681–706.

Notta, F., Chan-Seng-Yue, M., Lemire, M., Li, Y., Wilson, G.W., Connor, A.A., Denroche, R.E., Liang, S.B., Brown, A.M., Kim, J.C., et al. (2016). A renewed model of pancreatic cancer evolution based on genomic rearrangement patterns. Nature 538, 378–382.

Ouyang, H., Mou, Lj, Luk, C., Liu, N., Karaskova, J., Squire, J., and Tsao, M.S. (2000). Immortal human pancreatic duct epithelial cell lines with near normal genotype and phenotype. Am. J. Pathol. 157, 1623–1631.

Pannala, R., Leirness, J.B., Bamlet, W.R., Basu, A., Petersen, G.M., and Chari, S.T. (2008). Prevalence and clinical profile of pancreatic cancer-associated diabetes mellitus. Gastroenterology 134, 981–987.

Polak, P., Karlić, R., Koren, A., Thurman, R., Sandstrom, R., Lawrence, M., Reynolds, A., Rynes, E., Vlahoviček, K., Stamatoyannopoulos, J.A., et al. (2015). Cell-of-origin chromatin organization shapes the mutational landscape of cancer. Nature 518, 360–364.

Pylayeva-Gupta, Y., Grabocka, E., and Bar-Sagi, D. (2011). RAS oncogenes: weaving a tumorigenic web. Nat. Rev. Cancer 11, 761–774.

Qian, K., Wang, S., Fu, M., Zhou, J., Singh, J.P., Li, M.D., Yang, Y., Zhang, K., Wu, J., Nie, Y., et al. (2018). Transcriptional regulation of O-GlcNAc homeostasis is disrupted in pancreatic cancer. J. Biol. Chem. 293, 13989–14000.

Schirmer, M., Ijaz, U.Z., D'Amore, R., Hall, N., Sloan, W.T., and Quince, C. (2015). Insight into biases and sequencing errors for amplicon sequencing with the Illumina MiSeq platform. Nucleic Acids Res. 43, e37.

Schultz, L.B., Chehab, N.H., Malikzay, A., and Halazonetis, T.D. (2000). p53 binding protein 1 (53BP1) is an early participant in the cellular response to DNA double-strand breaks. J. Cell Biol. 151, 1381–1390.

Schuster-Böckler, B., and Lehner, B. (2012). Chromatin organization is a major influence on regional mutation rates in human cancer cells. Nature 488, 504–507.

Siegel, R.L., Miller, K.D., and Jemal, A. (2016). Cancer statistics, 2016. CA Cancer J. Clin. 66, 7–30.

Stamatoyannopoulos, J.A., Adzhubei, I., Thurman, R.E., Kryukov, G.V., Mirkin, S.M., and Sunyaev, S.R. (2009). Human mutation rate associated with DNA replication timing. Nat. Genet. 41, 393–395.

Su, M.A., Huang, Y.T., Chen, I.T., Lee, D.Y., Hsieh, Y.C., Li, C.Y., Ng, T.H., Liang, S.Y., Lin, S.Y., Huang, S.W., et al. (2014). An invertebrate Warburg effect: a shrimp virus achieves successful replication by altering the host metabolome via the PI3K-Akt-mTOR pathway. PLoS Pathog. 10, e1004196.

Surwit, R.S., Feinglos, M.N., Rodin, J., Sutherland, A., Petro, A.E., Opara, E.C., Kuhn, C.M., and Rebuffe-Scrive, M. (1995). Differential effects of fat and sucrose on the development of obesity and diabetes in C57BL/6J and A/J mice. Metabolism 44, 645–651.

Tape, C.J., Ling, S., Dimitriadi, M., McMahon, K.M., Worboys, J.D., Leong, H.S., Norrie, I.C., Miller, C.J., Poulogiannis, G., Lauffenburger, D.A., et al. (2016). Oncogenic KRAS regulates tumor cell signaling via stromal reciprocation. Cell *165*, 1818.

Valdiglesias, V., Giunta, S., Fenech, M., Neri, M., and Bonassi, S. (2013). γH2AX as a marker of DNA double strand breaks and genomic instability in human population studies. Mutat. Res. *753*, 24–40.

Vigneri, P., Frasca, F., Sciacca, L., Pandini, G., and Vigneri, R. (2009). Diabetes and cancer. Endocr. Relat. Cancer *16*, 1103–1123.

Waters, A.M., and Der, C.J. (2018). KRAS: the critical driver and therapeutic target for pancreatic cancer. Cold Spring Harb. Perspect. Med. *8*.

Wellen, K.E., and Thompson, C.B. (2010). Cellular metabolic stress: considering how cells respond to nutrient excess. Mol. Cell *40*, 323–332.

Wu, H.H., Hwang-Verslues, W.W., Lee, W.H., Huang, C.K., Wei, P.C., Chen, C.L., Shew, J.Y., Lee, E.Y., Jeng, Y.M., Tien, Y.W., et al. (2015). Targeting IL-17B-IL-17RB signaling with an anti-IL-17RB antibody blocks pancreatic cancer metastasis by silencing multiple chemokines. J. Exp. Med. *212*, 333–349.

Yang, X., and Qian, K. (2017). Protein O-GlcNAcylation: emerging mechanisms and functions. Nat. Rev. Mol. Cell Biol. *18*, 452–465.

Ying, H., Kimmelman, A.C., Lyssiotis, C.A., Hua, S., Chu, G.C., Fletcher-Sananikone, E., Locasale, J.W., Son, J., Zhang, H., Coloff, J.L., et al. (2012). Oncogenic Kras maintains pancreatic tumors through regulation of anabolic glucose metabolism. Cell *149*, 656–670.

Zeman, M.K., and Cimprich, K.A. (2014). Causes and consequences of replication stress. Nat. Cell Biol. *16*, 2–9.

STAR★METHODS

KEY RESOURCES TABLE

REAGENT OR RESOURCE	SOURCE	IDENTIFIER
Antibodies		
Phospho-Histone H2A.X (Ser139) (20E3)	Cell Signaling Technology	Cat# 9718 RRID:AB_2118009
O-GlcNAc (CTD110.6)	Cell Signaling Technology	Cat# 9875 RRID:AB_10950973
GLUT1	Proteintech	Cat# 21829-1-AP RRID:AB_10837075
GLUT2	Proteintech	Cat# 20436-1-AP RRID:AB_2750600
SGLT2	Proteintech	Cat# 24654-1-AP RRID:AB_2750601
SGLT1	Abcam	Cat# ab14686 RRID:AB_301411
p53R2 (RRM2B)	Abcam	Cat# ab154194 RRID:AB_2750599
O-linked N-Acetylglucosamine (RL2)	Abcam	Cat# ab2739 RRID:AB_303264
Pan-Ras Asp[12] (Ab-1)	Merck Millipore	Cat# PC10L RRID:AB_213468
Phospho-Histone H2A.X (Ser139)	Merck Millipore	Cat# 05-636 RRID:AB_309864
53BP1	Merck Millipore	Cat# MAB3802 RRID:AB_11212586
RRM1	Santa Cruz Biotechnology	Cat# sc-11733 RRID:AB_2180388
RRM2	Santa Cruz Biotechnology	Cat# sc-10844 RRID:AB_670992
GFAT1 (H49)	Santa Cruz Biotechnology	Cat# sc-134894 RRID:AB_10608981
Flag	Sigma-Aldrich	Cat# F3165 RRID:AB_259529
O-GlcNAc transferase (DM-17)	Sigma-Aldrich	Cat# O6264 RRID:AB_532313
PFKL	GeneTex	Cat# GTX105697 RRID:AB_1951188
PFKM	GeneTex	Cat# GTX111597 RRID:AB_1951192
PFKP	GeneTex	Cat# GTX107857 RRID:AB_2037665
His	GeneTex	Cat# GTX628914 RRID: AB_2750602
mCherry	GeneTex	Cat# GTX128508 RRID:AB_2721247
p84	GeneTex	Cat# GTX70220 RRID:AB_372637
GAPDH	GeneTex	Cat# GTX627408 RRID:AB_11174761
β-actin	GeneTex	Cat# GTX629630 RRID:AB_2728646
Chemicals		
D-(+)-Glucose	Sigma-Aldrich	Cat# G7021
adenosine	Sigma-Aldrich	Cat# A9251
uridine	Sigma-Aldrich	Cat# U3750
guanosine	Sigma-Aldrich	Cat# G6264
cytidine	Sigma-Aldrich	Cat# C4654
deoxyadenosine	Sigma-Aldrich	Cat# D7400
thymidine	Sigma-Aldrich	Cat# T1895
deoxyguanosine	Sigma-Aldrich	Cat# D0901
deoxycytidine	Sigma-Aldrich	Cat# D3897
CDP	Sigma-Aldrich	Cat# 30290
dCDP	Sigma-Aldrich	Cat# D7250

(*Continued on next page*)

Continued

REAGENT OR RESOURCE	SOURCE	IDENTIFIER
CTP-$^{13}C_9$	Sigma-Aldrich	Cat# 711020
Alloxan	Sigma-Aldrich	Cat# A7413
N-Acetyl-D-glucosamine	Sigma-Aldrich	Cat# A3286
UDP-GlcNAc	Sigma-Aldrich	Cat# U4375
Hoechst 33342	Sigma-Aldrich	Cat# B2261
collagenase IA	Sigma-Aldrich	Cat# C0130
HBSS	Sigma-Aldrich	Cat# H6648
Hepes	Sigma-Aldrich	Cat# H4034
Lipofectamine 2000 transfection reagent	ThermoFisher	Cat# 11668027
ProLong Gold Antifade Mountant with DAPI	ThermoFisher	Cat# P36935
2-NBDG	ThermoFisher	Cat# N13195
Soybean Trypsin inhibitor, powder	ThermoFisher	Cat# 17075029
EGF	ThermoFisher	Cat# PHG0311
blasticidin	ThermoFisher	Cat# A1113903
puromycin	ThermoFisher	Cat# A1113803
Rat Tail collagen I	CORNING	Cat# 354236
Ni-NTA agarose	GE Healthcare Life Sciences	Cat# 17-5318-01
Sephadex G-25 (particle size 100-300 μm)	GE Healthcare Life Sciences	Cat# 27532501
sWGA beads	Vector Laboratories	Cat# L-1020S
[^{3}H]dATP	Moravek	Cat# MT644
[^{3}H]dTTP	Perkin Elmer	Cat# PK-NET221H
blood glucose test strips	Roche, Indianapolis, IN	
Critical Commercial Assays		
Glucose-6-Phosphate Dehydrogenase (G6PDH) Assay Kit	Sigma-Aldrich	Cat# MAK015
Aldolase Activity Colorimetric Assay Kit	Sigma-Aldrich	Cat# MAK223
Phosphofructokinase (PFK) Activity Colorimetric Assay Kit	Sigma-Aldrich	Cat# MAK093
NADP/NADPH Quantification Kit	Sigma-Aldrich	Cat# MAK038
Cell Proliferation Kit II (XTT)	Roche, Indianapolis, IN.	Cat# 11465015001
Deposited Data		
Excel files for NGS data and Raw Tiff files for WB data	This paper	https://data.mendeley.com/datasets/478dxnw9zh/1 [doi:https://doi.org/10.17632/478dxnw9zh.1]
Experimental Models: Cell Lines		
HPDE (Ouyang et al., 2000)	a gift from Dr. Kelvin K. Tsai, National Health Research Institutes, Taiwan	https://www.ncbi.nlm.nih.gov/pmc/articles/PMC1885733/pdf/2396.pdf
HPNE	ATCC	Cat# CRL-4023, RRID:CVCL_C466
NL-20	ATCC	Cat# CRL-2503, RRID:CVCL_3756
MCF10A	ATCC	Cat# CRL-10317 RRID:CVCL_0598
H184B5F5/M10	BCRC	Cat# 60197, RRID:CVCL_Y093
NCM356	INCELL	RRID:CVCL_D875
HS68	BCRC	Cat# 60038, RRID:CVCL_0839
Mouse primary pancreatic acinar cells	This paper	N/A
Experimental Models: Organisms/Strains		
C57BL/6JNarl mice	Taiwan National Laboratory Animal Center	N/A

(Continued on next page)

Continued		
REAGENT OR RESOURCE	SOURCE	IDENTIFIER
Oligonucleotides		
For a complete list of shRNA-targeting sequences and oligos for PCR, qPCR, site-directed mutagenesis, and next-generation sequencing (NGS), see Table S1	This paper	Table S1
Software and Algorithms		
FlowJo 7.6.2	FlowJ	https://www.flowjo.com/
Prism 5	GraphPad Software	https://www.graphpad.com/

CONTACT FOR REAGENT AND RESOURCE SHARING

Further information and requests for resources and reagents should be directed to the Lead Contact, Chun-Mei Hu (cmhu1220@gate.sinica.edu.tw).

EXPERIMENTAL MODEL AND SUBJECT DETAIL

Ethics Statement
All pancreatic cancer tissue specimens were from the National Taiwan University Hospital, Taipei, Taiwan. All patients were given informed consent, which was approved by the Institutional Review Board of the NTUH (201303029RINC) and NTUH (201411085RINB).

Human Specimens
All male PDAC patients, in age from 43 to 79 years old, had anatomically resectable PDAC (TNM stages I and II). In addition, all patients with DM had at least 5 years with DM prior to PDAC diagnosis. The non-tumor regions of pancreatic and intestinal tissues used for the study were judged by cell morphology with Hematoxylin and Eosin (H&E) staining by an experienced clinical pathologist.

Animal Protocols, Diets, and Treatment
All experiments using animals were approved by the Institutional Animal Care and Utilization Committee of Academia Sinica, Taipei, Taiwan (IACUC#10-04-065). Male C57BL/6JNarl mice at the age of 4 weeks were obtained from the National Laboratory Animal Center (Taiwan). **Unless specified otherwise, mice were maintained in a SPF (specific pathogen-free) animal facility at 20±2 °C with a 12/12 hr light/dark cycle and had free access to water and standard laboratory chow diet.** For establishing the hyperglycemia model, mice (n=72) with similar body weight and blood glucose levels were randomly allocated to two groups: one group was fed a chow diet (13% calorie from fat, LabDiet 5010) and another was fed a high-sucrose (17.5%) and high-fat (35.8%) diet (HS/HF diet, TestDiet 58R3). A blood glucose meter (Roche Life Science) was used to monitor the level of blood glucose every week. Twelve mice from each group were sacrificed at 5, 10, and 20 weeks after feeding. Pancreatic, small intestinal, colon, liver, lung, and kidney tissue samples were collected, fixed in 10% paraformaldehyde, embedded in paraffin, and cut into 5 μm sections for immunohistochemistry analysis.

Sample Size Estimation
We chose our sample sizes based on those commonly used in this field without predetermination by statistical methods. This is stated in the figure legends.

General Cell Culture and Establishment of Stable Cell Lines
All cells were maintained at 37°C in a humidified atmosphere containing 5% CO_2. The non-transformed human pancreatic ductal epithelial cells (HPDE) generated from a 75-years old male pancreatic specimen (a gift from Dr. Kelvin K. Tsai, National Health Research Institutes, Taiwan) were grown in keratinocyte serum-free (KSF) medium with 0.2 ng/ml EGF and 30 μg/ml bovine pituitary extract (Invitrogen Life Technologies). The non-transformed human pancreatic acinar-to-ductal epithelial-like cells (HPNE) generated from a 52-years old male pancreatic specimen and non-transformed lung epithelial cells (NL20) generated from a 20-years old female lung specimen were obtained from Dr. Michael Hsiao at the Genomics Research Center, Academia Sinica, Taiwan. HPNE cells were grown in a medium containing one volume of M3[TM] base medium (INCELL) and three volumes of glucose-free DMEM supplemented with 5% FBS, 5.5 mM glucose, 10 ng/ml EGF, and antibiotics (penicillin/streptomycin). NL-20 cells were grown in a medium containing one volume of glucose-free DMEM and one volume of F12 medium supplemented with 0.1 mM nonessential amino acids, 0.005 mg/ml insulin, 10 ng/ml EGF, 0.001 mg/ml transferrin, 500 ng/ml hydrocortisone, 4% fetal bovine serum and antibiotics (penicillin/streptomycin). The non-transformed human mammary epithelial cells (MCF-10A) generated from a 36-years old female

mammary gland were grown in a medium containing one volume of glucose-free DMEM and one volume of F12 medium supplemented with 5% (vol/vol) donor horse serum, 20 ng/mL epidermal growth factor, 10 μg/mL insulin, 0.5 μg/mL hydrocortisone, 100 ng/mL cholera toxin, and antibiotics (penicillin/streptomycin).

The non-transformed mammary epithelial cells (H184B5F5/M10) generated from a 21-years old female mammary gland and non-transformed colon epithelial cells (NCM356) generated from a 65-years old male colon tissue were grown in MEM medium and M3^{TM} base medium (INCELL) supplemented with 10% FBS and antibiotics (penicillin/streptomycin), respectively.

The non-transformed foreskin fibroblast cells (HS68) generated from newborn male foreskin tissue were grown in low glucose (5.5 mM) DMEM medium supplemented with 10% FBS and antibiotics (penicillin/streptomycin). All cell lines were regularly checked for mycoplasma infection. For regular glucose treatment, cell medium was refreshed every 36 hours, and cells were replated every 72 hours to avoid over-crowding. For high-glucose treatment, ribonucleosides (N) addition and deoxynucleosides (dN) addition, cell medium was refreshed every 36 hours.

To establish the cell line that stably expresses the vector control, RRM1-WT, or RRM1-T734A, HPDE and HPNE cells were infected with the lentivirus containing the indicated cDNA and were selected with 2 μg/ml blasticidin. To establish the cell line that stably expresses LacZ^{shRNA} or OGT^{shRNA}, HPDE and HPNE cells were infected with the lentivirus containing the indicated shRNA and were selected with 1 μg/ml puromycin. To establish the cell line that stably expresses LacZ^{shRNA} or PFKL^{shRNA}, MCF-10A cells were infected with the lentivirus containing the indicated shRNA and were selected with 2 μg/ml puromycin. To establish the cell line that stably expresses LacZ^{shRNA} or GFPT1^{shRNA}, HPDE cells were infected with the lentivirus containing the indicated shRNA and were selected with 1 μg/ml puromycin. To establish the cell line that stably expresses LacZ^{shRNA}, GLUT1^{shRNA}, GLUT2^{shRNA}, SGLT1^{shRNA}, or SGLT2^{shRNA}, HPNE cells were infected with the lentivirus containing the indicated shRNA and were selected with 1 μg/ml puromycin. To establish the cell line that stably expresses the vector control or GLUT1, MCF10A cells were infected with the lentivirus containing the indicated cDNA and were selected with 2 μg/ml blasticidin.

Mouse Primary Pancreatic Acinar Cell Culture

Mouse primary acinar cells were isolated and cultured as described in Gout et al. (2013) (Gout et al., 2013). Briefly, all procedures for isolating acinar cells were performed under sterile conditions. Pancreases from 8-week-old male mice were mechanically and enzymatically digested with collagenase IA solution (1x HBSS containing 10 mM Hepes, 200 units/ml of collagenase IA, and 0.25 mg/ml of trypsin inhibitor) to obtain isolated acinar structures. Acini were grown in a medium containing one volume of glucose-free DMEM and one volume of F12 medium supplemented with 2.5 % FBS, 1% penicillin/streptomycin mixture, 0.25 mg/ml of trypsin inhibitor, and 25 ng/ml of recombinant human epidermal growth factor (EGF). After culturing on type I collagen-coated six-well culture dishes for 6 days, acinar to ductal-like cells were trypsinized and replated into another type I collagen-coated plate for subsequent experiments.

METHODS DETAILS

Plasmids, Construction of Expression Plasmids, and Site-Directed Mutagenesis

The lentiviral shRNA expression vectors of pLKO.1-shLacZ, shOGT (TRCN35064, 35067), shPFK (TRCN342355), and shGFAT1 (TRCN75219, TRCN 75220) were from the National RNAi Core Facility (Taipei, Taiwan). pET28a-RRM1 and pET28a-RRM2 were kindly provided by Dr. Yun Yen at Taipei Medical University, Taipei, Taiwan. pCMV2-RRM1, pAS3w-mCherry-RRM2, and pAS3w-mCherry-RRM2B was kindly provided by Dr. Zee-Fen Chang at National Taiwan University, Taipei, Taiwan. E. coli BL21 Tuner (DE3) GST-OGT-WT and H568A competent cells were kindly provided by Dr. Hsiu-Ming Shih at the Institute of Biomedical Sciences in Academia Sinica, Taipei, Taiwan. The retroviral cDNA expression vectors of pWZL-Neo-Myr-Flag-PFKL and PFKM were from Addgene.

pET28a-RRM2B was constructed by insertion of cDNA of RRM2B at BamHI site and EcoRI site of pET28a vector. The pCMV2-RRM1 (S253A, S616A, T734A, and S764A) mutant was generated using a QuickChange XL site-directed mutagenesis kit (Stratagene). pAS5w-RRM1-WT, pAS5w-RRM1-T734A, and pAS5w-GLUT1 were constructed by insertion of cDNA of RRM1 and GLUT1 at NheI and EcoRV sites of the pAS5w.bsd vector, respectively.

Immunohistochemistry (IHC)

IHC was performed on a BenchMark Ultra auto-stainer (Ventana Medical Systems). Sections were deparaffinized with EZPrep buffer (Ventana Medical Systems), and antigen retrieval was also performed in this instrument. Slides were incubated with anti-γH2AX antibody (1:100, Cell Signaling #9718) or anti-O-linked N-Acetylglucosamine antibody [CTD 110.6] (1:100, Cell Signaling #9875) for 4 hours followed by 1-hour incubation with secondary antibody. Then slides were processed with a DAB detection kit (Ventana Medical Systems) and counterstained with haematoxylin (Ventana Medical Systems). For IHC data analysis, slides were scanned at 40× magnification using Aperio Digital Pathology Slide Scanners and the images of high power field at 40× magnification were randomly selected and analyzed by Leica Aperio Imagescope digital slide viewer v9.1.19.1568. Quantification of γH2AX and O-GlcNAc per sample was determined by analyzing 50 randomly chosen high-power fields (HPF), 40x magnification, and performed by Aperio IHC Nuclear Algorithm and Aperio Positive Pixel Count, respectively.

Immunofluorescence Staining

For γH2AX and 53BP1 foci staining, cells grown on coverslips or culture dishes were fixed with 4% paraformaldehyde and permeabilized with 0.3% Triton X-100 in TBS (50 mM Tris-HCl, pH 7.4, 150 mM NaCl) buffer. For KRAS^{G12D} staining, cells grown on coverslips were washed with CSK (100 mM NaCl, 300 mM sucrose, 10 mM PIPES pH 7.0, 3 mM MgCl$_2$, 0.1% of Triton X-100) buffer twice and then fixed with 4% paraformaldehyde, permeabilized with 0.3% Triton X-100 in TBS buffer. Cells were blocked with MAXblock^{TM} (Active Motif) for 1 hour at 37°C, followed by staining with anti-γH2AX (1:1000, Merck Millipore #05-636), anti-53BP1 (1:1,000, Merck Millipore #MAB3802), or anti-KRAS^{G12D} (100 ng/μl, 1:100, Merck Millipore # PC10L) at 4°C overnight. After extensive washing, these cells were stained with Alexa Fluor 488-conjugated secondary antibodies for 1 hour at room temperature. After wash, cells were stained with DAPI (10 μg/ml, 1:1000, Life Technologies) and mounted with ProLong Gold Antifade Mounting Oil. The percentage of γH2AX and 53BP1 foci-positive cells was determined by analyzing 2,000 randomly chosen cells with Cellomics ArrayScan VTI and the foci-positive cells were defined as nuclei with at least one large focus or a granular pattern of green fluorescence.

Soft Agar Colony Formation Assay

Soft agar colony formation assay was performed by seeding 10^4 cells in a layer of 0.35% agar/complete growth medium over a layer of 0.5% agar/complete growth medium in the wells of a 12-well plate. Cell medium containing the indicated concentration of glucose, nucleosides, deoxynucleosides, or Alloxan (Sigma-Aldrich) was replenished every 3 days. Cultures were maintained in a humidified 37°C incubator. On day 21 or day 27 after seeding, cells were fixed with pure ethanol containing 0.05% Crystal Violet (crystal violet (Sigma-Aldrich C3886), and the colony-forming efficiency was quantified under a light microscopy. Colonies, which size was quantified by the diameter of each colony, larger than 50 μm were counted and analyzed.

Glucose Metabolite Analysis

Following culture with the indicated concentrations of glucose for 3, 9, or 27 days, cells were washed twice with PBS and harvested with nuclease-free water. The samples were collected, sonicated with amplitude 80% around 30 sec (Hielscher, Ultrasound Technology), and then centrifuged at 10,000 g for 10 min. 100% acetone nitrate was added to the supernatant at a ratio of 1:3. After being centrifuged again at 10,000 g for 10 min, the supernatant was lyophilized and the pellet was dissolved in 35 μl ddH2O for LC-ESI/MS metabolomic analysis described as follows by Su et al. (Su et al., 2014).

To enhance the detection of the carboxylic acid and organic phosphate signals, 5 μl aniline/HCl reaction buffer (0.3 M aniline [Sigma-Aldrich, USA] in 60 mM HCl) and 5 μl of 20 mg/ml N - (3-dimethylaminopropyl)-N′-ethylcarbodiimide hydrochloride (EDC; Sigma-Aldrich, USA) were added to each sample of the hemocyte residue. Each mixture was vortexed and incubated at 25°C for 2 h, after which the reaction was stopped by adding 5 μl of 10% ammonium hydroxide. The aniline derivatized samples were then analyzed using an LC-ESI-MS system consisting of an ultra-performance liquid chromatography (UPLC) system (Ultimate3000 RSLC, Dionex) and a quadrupole time-of-flight (TOF) mass spectrometer with an the electrospray ionization (ESI) source (maXis UHR-QToF system, Bruker Daltonics). The cells metabolites were separated by reversed-phase liquid chromatography (RPLC) on a BEH C18 column (2.1×100 mm, Walters). The LC parameters were as follows: autosampler temperature, 4°C; injection volume, 10 μl; and flow rate, 0.4 ml/min. After pre-starting with 1% mobile phase B (0.1% formic acid in ACN) for 4 min, the elution started from 99% mobile phase A (0.1% formic acid in ddH2O) and 1% mobile phase B (0.1% formic acid in ACN). After holding at 1% for 0.5 min and raising to 60% over 5 min, mobile phase B was further raised to 90% in another 0.5 min, held at 90% for 1.5 min, and then lowered back to 1% in 0.5 min. The column was then equilibrated by pumping 99% B for 4 min. The acquisition parameters for LC-ESI-MS chromatograms were as follows: dry gas temperature, 190°C; dry gas flow rate, 8 L/min; nebulizer gas, 1.4 bar and capillary voltage, 3,500 V. Mass spectra were recorded from m/z 100–1000 in the negative ion mode. Data were acquired by HyStar and microTOF control software (Bruker Daltonics) and processed by DataAnalysis and TargetAnalysis software (Bruker Daltonics). Each metabolite was identified by matching with its theoretical m/z value and with the isotope pattern derived from its chemical formula. The identified metabolites were quantified by summing the corresponding area of the extracted ion chromatogram.

Cellular dNTP Extraction and Quantification

dNTPs from 2×10^6 cells were extracted with 1 ml of ice-cold 60% methanol, followed by centrifugation for 30 min at 16,000 g. The supernatant was immersed at 100°C in a dry bath for 3 min and dried under vacuum. The pellets were dissolved in nuclease-free water for dNTP measurement based on the method described as follows by Ferraro et al. (Ferraro et al., 2010).

Briefly, the reaction mixture contained, in a volume of 0.1 ml, 0.1–4 pmol of the dNTP to be determined together with 40 mM Tris-HCl, pH 7.4, 10 mM MgCl$_2$, 5 mM dithiothreitol, 0.25 μM oligonucleotide, 1.5 μg RNase A, 0.25 μM labeled dATP, 500–1000 cpm/pmol (or labeled dTTP for the dATP assay) and DNA polymerase. RNase A was included in the assay to remove any labeled RNA formed in metabolic experiments with ^{3}H- labeled nucleosides. The nature and the amount of the DNA polymerase used in the assay are given below for each separate dNTP determination. After 60 min incubation 0.085 ml of the mix was spotted on circular disks of Whatman DE81 paper. After drying, the filters were washed three times for 10 min in large volumes of 5% Na$_2$HPO$_4$, once in distilled water and once in absolute ethanol. The retained radioactivity was determined by scintillation counting.

We used limiting amounts of the Klenow enzyme for dTTP and dATP assays and the Taq DNA polymerase for dCTP and dGTP assays. The chosen enzyme concentration must be balanced by the requirement of a close to linear dose–response curve in the range of the dNTP concentrations to be analyzed. It is advisable to test each new batch of enzyme to find the smallest amount of enzyme that for a given dNTP suffices to give a close to linear standard curve between 0.1 and 4 pmol of the dNTP. We found

this range to be optimal for the analysis of dNTPs present in cell extracts. For our Klenow enzyme 0.2 units sufficed for the dTTP assay and 0.025 units for the dATP assay, with 60 min incubation at 37°C. For Taq DNA polymerase 2 units were required for both dCTP and dGTP, with 60 min incubation at 48°C. Once standardized, we used each batch of enzyme for months without change of conditions and without interference by rNTPs.

Analysis of UDP-GlcNAC Using Liquid Chromatography-Mass Spectrometry (LC-MS)

For UDP-GlcNAC analysis, a linear ion trap-orbitrap mass spectrometer (Orbitrap Elite, Thermo Fisher Scientific, Bremen, Germany) coupled online with an ultrahigh performance liquid chromatography (UHPLC) system (ACQUITY UPLC, Waters, Millford, MA) was used. The mass spectrometer was operated in the negative ion mode and set to one full FT-MS scan (m/z 150-615, resolution = 15,000) and two FT-MS product ion scans for precursors of UDP-GlcNAC (precursor m/z = 606.08, m/z 150-615, 15,000 resolution) and CTP-13C9 (precursor m/z = 491.03, m/z 300-500, 15,000 resolution). The sample was loaded into the UHPLC system and separated by a HILIC column (BEH Amide, 1.7 μm, 2.1 mm × 100 mm, Waters, Milford, MA), which coupled directly to a mass spectrometer. The solvent A with 20 mM ammonium acetate in 40% ACN with pH = 9 and solvent B with pure ACN were used as the mobile phase for UHPLC separation. The solvent gradient in UHPLC separation was started from 60-99.9% solvent A at 0-3 minutes at a flow rate of 400 μl/min. The total chromatography separation time for each of the analyses was 7 minutes. The fragmentation reactions of m/z 606.08 to 384.99 for UDP-GlcNAC and 491.03 to 393.03 for CTP-13C9 were selected for quantitation using the chromatographic peak area in selected ion chromatogram (SIC). The relative abundance of UDP-GlcNAC was quantified by the abundance of dope CTP-$^{13}C_9$.

Cellular RNR Activity Analysis

RNR activity analysis was performed and modified as previously described (Jong et al., 1998). Cells were incubated with growth medium containing the indicated concentrations of glucose for 3 days, and then 2.5×10^6 cells were trypsinized and homogenized in 500 μl of buffer I (50 mM Hepes, pH 7.2; 2 mM DTT, 0.2 mg RNaseA) on ice. After centrifugation at 16,000 g for 15 min, the supernatant was applied onto a Sephadex G-25 spin column, which had been pre-equilibrated with ice-cold buffer II (50 mM Hepes, pH 7.2; 2 mM DTT). The loaded spin column was centrifuged at 1,500 g for 5 min, and the pass-through sample was collected for the RNR activity assay. Protein concentration was measured by using the kit from BioRAD-based Bradford method. Approximately 150 μg protein was used per RNR assay.

The RNR assay mixture contained 50 mM Hepes, pH 7.2, 6 mM DTT, 4 mM Mg acetate, 2 mM ATP, and 1 μM CDP. The reaction was initiated by adding RNA-free crude extracts and incubated at 37°C for 30 min, and the reaction was terminated at 100°C in a dry bath for 5 min. The substrate CDP was converted to dCDP by RNR and subsequently to dCTP by endogenous NDP kinase in the reaction mixture. After centrifugation at 16,000 g for 5 min, the supernatant was dried under vacuum and dissolved in 16 μl of nuclease-free water for dCTP level determination as described in dNTP quantification. Since RNR activity is the limiting step for dCTP formation in the reaction, the amount of dCTP formation can be represented as RNR activity.

NDPK Activity Analysis

Cell crude extracts preparation and enzyme reactions were similar to RNR activity analysis as described in STAR Methods. dCDP instead of CDP was used as the substrate for NDPK activity analysis.

PFK Activity Measurement

PFK activity was determined according to manufacturer's instructions (MAK093, Sigma-Aldrich). In brief, cells were incubated with growth medium containing the indicated concentrations of glucose for 3 or 9 days, and then cells were trypsinized and counted. 2×10^5 cells were homogenized in 200 μl of ice-cold PFK assay buffer. 1/100 dilution of sample was used for subsequent activity assay. PFK activity was reported as nmole/min/mL (milliunit/mL). One unit of PFK is the amount of enzyme that generates 1.0 μmole of NADH per minute at pH 7.2 at 37 °C.

sWGA Pull-Down Assay

sWGA (succinylated wheat germ agglutinin) is a modified lectin that specifically binds O-GlcNAc on proteins. Pancreatic cells and mammary cells were lysed in Lysis 125 buffer (50 mM Tris, pH 7.4, 125 mM NaCl, 5 mM EDTA, 5 mM EGTA, 0.1% Nonidet P-40, 50 mM NaF, 1 mM PMSF and 1x Proteinase Inhibitor Cocktail (Roche, Indianapolis, IN)). After being clarified by spinning at 15,000 rpm for 15 min, the supernatant was collected and incubated by sWGA beads with or without 0.5 M N-Acetyl-D-Glucosamine (GlcNAc). After overnight incubation at 4°C, the beads were washed three times with Lysis 125 buffer, and sWGA-bound proteins were eluted with Laemmli sample buffer for PFK isoforms and RNR subunits detection by immunoblotting.

Immunoprecipitation and Immunoblotting

For RRM1 immunoprecipitation, cells were lysed in RNR lysis buffer (50 mM Tris-HCl pH 7.5, 150 mM NaCl, 0.5% NP40, 50 mM NaF, 1 mM Na$_2$VO$_3$, 1 mM DTT, 0.1% SDS, 2 mM PMSF and protease inhibitors), and the supernatant was incubated with M2 beads at 4°C for 2 hours, or with anti-RRM1 antibody or anti-goat-IgG antibody at 4°C overnight followed by 1-hour incubation with Protein G beads. Beads were washed three times with RNR lysis buffer, and proteins were eluted with Laemmli sample buffer. Protein samples resolved by SDS-PAGE were transferred to PVDF membrane, and then incubated with primary antibody followed by horseradish

peroxidase (HRP)-conjugated IgG secondary antibodies (1:5,000, GeneTex). Signals were detected using Luminata Forte Western HRP Substrate (Merk Millipore, WBLUF0500).

Protein Purification
pET28a-RRM1, RRM2, or RRM2B plasmid was transformed into *E. coli* BL21 Tuner (DE3) GST-OGT-WT or GST-OGT-H568A competent cells. The single colony was cultured at 25°C to an OD_{600} of 0.6 in LB, and the desired protein was induced with 0.4 mM IPTG at 16°C overnight. Bacteria pellets were resuspended in lysis buffer (50 mM Tris-HCl, pH 7.5 and 250 mM NaCl) and then sonicated with amplitude 80% around 30 sec on ice (Hielscher, Ultrasound Technology). After centrifugation, the supernatant was incubated with Ni-NTA agaroses (Roche, Indianapolis, IN) for 1 hour at 4°C. His-tagged proteins were eluted with 300 mM imidazole, and then imidazole was removed by dialysis.

Protein In Vitro Binding Assay
1 μg of purified His-RRM1 or O-GlcNAc-His-RRM1 was mixed with HPDE or HPNE cell lysates in 0.5 ml of RNR lysis buffer for 1 hour under constant rotation at 4°C. Then Ni-NTA beads were added and incubated for 1 hour at room temperature. Ni-NTA beads (Roche, Indianapolis, IN) were then washed five times, and bound-proteins were analyzed by Western blotting.

Genomic DNA Extraction
Tumor-free regions of pancreatic and intestinal tissues from PDAC patients diagnosed with or without DM were collected from paraffin blocks according to pathologist's recognition. All samples were used for genomic DNA extraction following manufacturer's instructions (QIAamp DNA Mini kit, 51306).

Amplicon Library Preparation
Exon 2, 3, and 4 of *KRAS*, exon 9 of GAPDH gene, exon 2 of *Kras* gene and exon 4 of *Gapdh* gene were used for amplicon amplification and sequencing. The forward and reverse primers that are complementary upstream and downstream of the region of interest were designed with overhang adapters, and used to amplify templates from genomic DNA. A subsequent limited-cycle amplification step was performed to add multiplexing indices and Illumina sequencing adapters. Libraries were normalized and pooled as described by "16S Metagenomic Sequencing Library Preparation", and sequenced on the MiSeq system.

Sequencing with Illumina MiSeq and Data Analysis
The amplicon library was prepared for sequencing according to the manufacturer's instructions (MiSeq Sequencing protocol). In brief, the amplicon pool was pre-diluted to 2 nM and denatured. 10% of the denatured PhiX control (Illumina, # FC-110-3001) was spiked into the 6 pM amplicon pool and loaded to the sample reservoir of the MiSeq Reagent Cartridge. We used the 500-cycle v2 kit for amplicon sequencing. The run was set by using the MiSeq Control Software (MiSeq Reporter 2.2.29) according to the *MiSeq System User Guide Part* (# 15027617). A sample sheet (csv-file) for FASTQ format output was designed with the Illumina Experiment Manager 1.5. The run was performed for 2 x 250 bp using a paired-end approach, with automated cluster-generation, Sequencing-by-synthesis (SBS) included reversible terminator sequencing of the indexed samples, and producing demultiplexed FASTQ files. Total 896 bases in the regions of the amplicons including *KRAS* exon 2-4, total 329 bases in the regions of the amplicons including *GAPDH* exon 9, total 281 bases in the regions of the amplicons including *Kras* exon 2, and total 277 bases in the regions of the amplicons including Gapdh exon 4 were counted by bam-readcount (https://github.com/genome/bam-readcount). After that, the counts and frequencies of bases at each position in those regions were calculated. The data represent the average of single nucleotide variants.

Lentiviral shRNA, Lentiviral cDNA, and Retroviral cDNA Production for Infection
Lentiviral shRNA, lentiviral cDNA, and retroviral cDNA were packaged in 293T and 293GP2 cells, respectively. For lentivirus production, 293T cells ($5×10^6$ cells) were co-transfected with 3 μg of pCMVΔ8.91, pMD.G, and 3 μg of pLKO.1-indicated[shRNA] or pAS5w-indicated cDNA. For retrovirus production, 293GP2 cells ($5×10^6$ cells) were co-transfected with 4 μg of pWZL-Neo-Myr-Flag-PFKL/PFKM) and 4 μg of pMD.G. At 72 h after transfection, culture media containing lentivirus or retrovirus were collected and concentrated on a Millipore concentration column to a final volume of 1 ml. The lentiviral shRNA, lentiviral cDNA, and the retroviral cDNA stocks in 0.2 ml of medium containing 8 μg/ml polybrene were used to infect $2.5×10^5$ cells overnight, after which the media were replaced with complete medium for subsequent assays.

Cell Growth, Cell Cycle, and 2D Clonogenic Cell Survival Analysis
Cells plated into a 96-well plate (10^3 cells/well) were cultured with medium containing the indicated concentrations of glucose and cell growth was measured by the XTT assay (Roche). Cell cycle analysis was performed by staining cells with propidium iodide (PI), which was followed by fluorescence-activated cell sorter (FACS) analysis using CellQuest software (Bd Biosciences). 2D clonogenic cell survival assays were performed by seeding cells at a rate of 500 cells per well into a 6-well plate. After 14 days, the colonies were fixed and stained by Crystal Violet and counted.

Protein Extraction and Western Blotting Analysis

Cell extracts were prepared and equal amounts of protein were separated by NuPAGE™ 4-12% Bis-Tris Protein Gels (Thermo Fisher Scientific) followed by electrophoretic transfer to PVDF membranes (Millipore). After blocking with TOOLSpeed Blocking Reagent (TFU-BL500, TOOLS Taiwan) the membrane was incubated with different antibodies overnight at 4°C and treated for 1 hr with horse-radish peroxidase-conjugated goat anti-rabbit IgG, goat anti-mouse, and donkey anti-goat antibodies (Santa Cruz). ECL detection of the horseradish peroxidase reaction was performed according to the manufacturer's instructions (WBLUF0500, Merck Millipore). Protein signal was measured on a UVP BioSpectrum 500 Imaging System.

Cellular ROS Measurement

Following culture with the indicated concentrations of glucose for 3 or 9 days, culture media were removed, and cells were loaded with 5 μM H$_2$DCFDA diluted in clean medium for 30 min at 37°C. Cells were washed twice with PBS and trypsinized for flow cytometry (FACScalibur, BD Bioscience) analysis using the FL1 channel (Green fluorescence). The profile was examined by CellQuest software (BD Bioscience).

Analysis of NTPs Using Liquid Chromatography-Mass Spectrometry (LC-MS)

For NTP analysis, the mass spectrometer was operated in the negative ion mode and set to one full FT-MS scan (m/z 300-600, resolution = 15,000) and nine FT-MS product ion scans (m/z 300-600, 15,000 resolution) for precursors ATP (precursor m/z = 505.99), CTP (precursor m/z = 481.98), UTP (precursor m/z = 482.96), GTP (precursor m/z = 521.99) and CTP-13C9 (precursor m/z = 491.03). The sample was loaded into the UHPLC system and separated by a HILIC column (BEH Amide, 1.7 μm, 2.1 mm × 100 mm, Waters, Milford, MA), which coupled directly to a mass spectrometer. The solvent A with 20 mM ammonium acetate in 40 % ACN with pH = 9 and solvent B with pure ACN were used as the mobile phase for UHPLC separation. The solvent gradient in UHPLC separation was started from 30% solvent A at 0-1 minute, and 30-100% at 1-5 minutes at the flow rate of 400 μl/min. The total chromatography separation time for each of the analyses was 8 minutes. The fragmentation reactions m/z 507.18 to 409.20 for ATP, m/z 481.98 to 384.00 for CTP, m/z 482.96 to 384.99 for UTP, m/z 521.99 to 424.01 for GTP and 491.03 to 393.03 for CTP-^{13}C$_9$ were selected for quantitation using the chromatographic peak area in selected ion chromatogram (SIC). The relative abundance of NTP was quantified by the abundance of dope CTP-^{13}C$_9$.

Cellular NADPH Measurement

Cells were harvested after incubation with growth medium containing the indicated concentrations of glucose for 3 days. Cellular NADPH measurement was performed by NADP/NADPH Quantification Kit (MAK038, Sigma-Aldrich) following manufacturer's instructions.

G6PDH and Aldolase Activity Measurement

Cells were harvested for G6PDH and aldolase activity assay according to manufacturer's instructions (MAK015 and MAK223, respectively, Sigma-Aldrich) after 3 or 9 day-incubation with growth medium containing the indicated concentrations of glucose. G6PDH and aldolase activity were reported as nmole/min/mL (milliunit/mL). One unit of G6PDH or aldolase is the amount of enzyme that generates 1.0 μmole of NADH per minute at pH7.2 at 37 °C.

Glucose Uptake Assay

2 x 10^4 cells per well were seeded into a 96-well plate overnight. Then cells were washed twice with PBS and incubated with 2-NBDG at the indicated concentrations for 10 min or 100 μM 2-NBDG at the indicated time points at 37°C. The reaction was stopped by adding a two-fold volume of ice-cold PBS, and the cells were washed twice with ice-cold PBS. Fluorescence signals before (autofluorescence) and after adding 2-NBDG were measured by using the 485 nm$_{ex}$ and 520 nm$_{em}$ filter set in a multi-well plate reader (Victor-3, Perkin Elmer, Waltham, MA, USA). Cell number per well was determined by Cell Proliferation Kit (XTT assays, Roche, Indianapolis, IN) following manufacturer's instructions. The glucose uptake, indicated by fluorescent values, was normalized by the cell number.

To examine the effect of GLUT and SGLT on glucose uptake in human pancreatic cells, HPDE or HPNE cells were co-incubated with 100 μM 2-NBDG and 10 μM Cytochalasin B or 100 μM Phlorizin in medium containing 5.5 mM glucose. After 10 min, glucose uptake in cells was determined as described above.

Flow Cytometry for Cell Cycle Analysis

After high-glucose treatment for 3 days, cells (1 x 10^6) were fixed in ice-cold 70% ethanol at -20°C overnight. Then, cells were washed with ice-cold PBS once and resuspended in 1 ml of propidium iodide (PI) staining solution (0.1% Triton-x-100, 02 mg/ ml RNasa A and 20 μg/ ml PI). After incubation in dark condition at room temperature for 30 min, the cell cycle profile was examined by flow cytometry analysis (FACScalibur, BD Bioscience) with CellQuest software. For each measurement, data from 10,000 single cell events were collected. For analysis, we first gated on the single cell population using the pulse width vs. pulse area. Then we applied this gate to the scatter plot and gated out the obvious debris. Finally, we combined the gates and applied to the PI histogram plot.

Flow Cytometry for KRAS^{G12D} Analysis

The cells were fixed and permeabilized with ice-cold methanol (-20°C). Then, cells were incubated with or without the anti-KRAS^{G12D} antibody (200 ng / μl, 1:100) for 1 hour at 4°C, followed by staining with Alexa Fluor 488-conjugated secondary antibodies for 1 hour at 4°C. After wash, cells were used for flow cytometry analysis with CellQuest software. Cell debris was removed by gating the major population in a SSC vs FCS density plot.

Flow Cytometry for Glucose Uptake Analysis

5×10^5 cells were seeded in a 60-mm dish overnight. Then 100 μM of 2-NBDG was added and incubated at the indicated time points. After stopping the uptake reaction, cells in each dish were subsequently trypsinized and resuspended in 500 μl ice-cold growth medium for flow cytometry analysis with CellQuest software. Cell debris was removed by gating the major population in a SSC vs FCS density plot. For each measurement, data from 10,000 single cell events were collected.

In-Gel Digestion of Purified RRM1 Protein

The purified RRM1 proteins were separated by SDS-PAGE, and the band stained by Coomassie blue were excised, cut into smaller pieces, and destained by 50% acetonitrile (ACN) with 25 mM triethylammonium bicarbonate (TEABC). The proteins in the gel pieces were reduced by 5 mM tris (2-carboxyethyl) phosphine (TCEP) at 37°C for 30 min in the dark and alkylated by 20 mM iodoacetamide (IAM) at 37°C for 60 min in the dark. After extraction with 100% ACN and removing all liquid, the gel pieces were re-saturated with 25 mM TEABC, to which 2 μg trypsin was added, and were incubated at 37°C for 16 h. Digested peptides were extracted by 50% ACN/5% formic acid (FA) twice and 100% ACN and dried completely under vacuum. The peptides were desalted by C18 Zip-tip (Millipore) and subjected to LC-MS/MS analysis.

LC-MS/MS Analysis

The desalted peptides were resuspended with 0.1% FA and analyzed by Orbitrap Fusion Tribrid Mass Spectrometer (Thermo Fisher Scientific, San Jose, CA) equipped with a PicoView nanospray interface (New Objective, Woburn, MA). Peptides were loaded onto an analytical C18 column (Acclaim PepMap RSLC, 75 μm i.d. x 25 cm length; Thermo Fisher Scientific) packed with 2 μm particles with a pore size of 100 Å, and were separated using a segmented gradient for 120-min with the following mobile phases: water with 0.1% FA (buffer A) and 2% to 85% ACN with 0.1% FA (buffer B) at 500 nL/min flow rate. Survey scans of peptide precursors from 350 to 1550 m/z with charge states 2-6 were performed at 120K resolution and the AGC target was set to 2×10^5 by Orbitrap. Tandem MS was performed by isolation window at 2.0 Da with the quadrupole, AGC target to 1×10^5, and used for higher-energy collisional dissociation (HCD) fragmentation detected in Orbitrap at a resolution setting of 30K with a normalized collision engergy (NCE) of 26%. Product ion-dependent trigger was set with 204.0867 for HexNAc, 186.075 and 18.065 for HexNAc fragments to filter the O-GlcNAc-conjugated peptides for following MS2 dissociation by electron-transfer dissociation (ETD) or electron-transfer and higher-energy collision dissociation (EThcD). ETD and EThcD were performed at 30K resolution, isolation window at 1.4 Da with the quadrupole, the AGC target was set to 1 x 105 by Orbitrap, and used calibrated charge dependent ETD parameters. Top 20 of given precursors were selectively fragmented and scanned out in mass spectra.

Data Processing and Database Search

The raw data were processed by using Proteome Discoverer 2.0 (PD2.0; Thermo Fisher Scientific), and peptide identification was performed by Byonic search engine (version 2.9) against the RRM1 protein sequence with a percolator (strict false discovery rate (FDR) of 0.01 and a relaxed FDR of 0.05). The protease was specified as trypsin with 2 maximum missing cleavage sites. Mass tolerance for precursor ion mass was 10 ppm with the fragment ion tolerance as 20 ppm for HCD, ETD, and EThcD. Oxidation at methionine, carbamidomethyl at cysteine, deamidation at asparagine or glutamine, and HexNAc at serine or threonine were selected as variable modifications. Peptides were considered to be identified if their individual ion score was higher than the identity score ($p < 0.05$). To evaluate the false discovery rate ($< 1\%$) in protein identification, a decoy database search against a randomized decoy database created by PD2.0 using identical search parameters and validation criteria was also performed. Peptide-spectrum matches (PSMs) with at least high confidence and a strict maximum parsimony principle (target FDR <0.01) were applied for the protein level. All selected MSMS spectra of O-GlcNAc-modified peptides were manually confirmed.

Experiment Design

Replication

All experimental findings were reproduced in multiple independent experiments.

For each figure panel, the number of independent experiments or biological replicates is indicated in the figure legends. Data shown in figure panels are the mean ± SD of all independent biological or technical repeats. Western blot pictures are from a representative experiment and the number of independent repeats is clearly indicated in the figure legends.

Strategy for Randomization and/or Stratification

The age-matched mice with similar body weight and blood glucose level were randomly divided into each experimental group. This is stated in the "Animal protocols, diets and treatment".

Blinding at Any Stage of the Study

The investigators were not blinded to the group allocation during experiments and outcome assessment.

Sample-Size Extermination and Statistical Method of Computation

We chose our sample sizes based on those commonly used in this field without predetermination by statistical methods. This is stated in the figure legends. For all figures and tables that use statistical methods, we confirmed that the following items are present in relevant figure legends.

1. The exact sample size (n) for each experimental group/condition, given as a discrete number and unit of measurement (animals, litters, cultures, etc.)
2. A description of how samples were collected, noting whether measurements were taken from distinct samples or whether the same sample was measured repeatedly.
3. A statement indicating how many times each experiment was replicated.
4. The statistical test(s) used and whether they are one- or two-sided. Only common tests should be described solely by name; describe more complex techniques in the STAR Methods section.
5. A description of any assumptions or corrections, such as an adjustment for multiple comparisons
6. Test values indicating whether an effect is present. Provide confidence intervals or give results of significance tests (e.g. P values) as exact values whenever appropriate and with effect sizes noted.
7. A clear description of statistics including central tendency (e.g. median, mean) and variation (e.g. standard deviation, interquartile range).
8. Clearly defined error bars in all relevant figure captions (with explicit mention of central tendency and variation)

Inclusion and Exclusion Criterial of Any Data or Subjects

All samples/ animals that met proper experimental conditions were included in the analysis. No data were excluded from the analyses.

QUANTIFICATION AND STATISTICAL ANALYSIS

Statistical Analyses

A two-tailed Student's t-test was used for immunohistochemistry, immunostaining analysis, soft agar colony formation, NGS analysis, cellular dNTP and UDP-GlcNAc level determination, enzyme activity analysis, and RNR complex formation analysis. *, **, and *** indicate $p < 0.05$, $p < 0.01$, and $p < 0.001$, respectively. N number used in indicated section was shown in the figure legends.

DATA AND SOFTWARE AVAILABILITY

Excel files for NGS data and raw Tiff files for WB data have been deposited in Mendeley: https://data.mendeley.com/datasets/478dxnw9zh/1 DOI: https://doi.org/10.17632/478dxnw9zh.1

The information for FlowJo 7.6.2 and Prism 5 soft wares are included in the Key Resources Table.